MULTI-WAVELENGTH ANALYSIS OF 13 UNKNOWN GALACTIC FERMI GAMMA-RAY SOURCES

by

Brice Michael Williams, B.S., B.S.

A thesis submitted to the Graduate Council of
Texas State University in partial fulfillment
of the requirements for the degree of
Master of Science
with a Major in Physics
May 2022

Committee Members:

Blagoy Rangelov, Chair

Andrea Banzatti

Aditya Togi

FAIR USE AND AUTHOR'S PERMISSION STATEMENT

DEDICATION

To my family for constantly reminding me that I can accomplish anything I set my mind to. I would also like to thank them for reminding me that it’s never too late to go back to school in the pursuit of my dreams.

ACKNOWLEDGEMENTS

I am deeply thankful to Dr. Blagoy Rangelov, my advisor, for taking me on as a research assistant and for his mentorship as I start my journey into the profession of astrophysicist. His guidance on my thesis research project and in my development of the skills needed for a successful career are invaluable. Special thanks to Dr. Wilhelmus Geerts for encouraging me to apply to Texas State's physics master's program: without his encouragement, none of this would have been possible. I would also like to thank my committee members, Dr. Andrea Banzatti and Dr. Aditya Togi, for their support and advice on how to succeed in a doctorate program.

Thanks to the various research centers that provided tools, training on analysis, and data used in this thesis. These include the Chandra X-ray Center (CXC), the High Energy Astrophysics Science Archive Center (HEASARC), and the observatories used for the multi-wavelength data: GAIA, 2MASS, WISE, and PanSTARRS. The CXC provided the CIAO software package and analysis threads used to process the data. HEASARC provided the XSPEC tool for modeling X-ray spectra as well as the known hydrogen column densities for our observations' location.

Lastly, I would like to thank my grandma and her husband for their support during my time at Texas State. I have immensely enjoyed getting to spend so much time over the past two years together.

TABLE OF CONTENTS

Page

ACKNOWLEDGEMENTS v

LIST OF TABLES viii

LIST OF FIGURES ix

LIST OF ABBREVIATIONS xi

ABSTRACT xviii

CHAPTER

I. INTRODUCTION 1

I.a. History of Gamma-ray Astronomy 1
I.b. Why Multi-wavelength? 4

II. TYPES OF X-RAY OBJECTS 9

II.a. Supernova and Supernova Remnants 10
II.b. Neutron Stars 14
II.b.i. Pulsars 15
II.b.ii. Pulsar Wind Nebulae 16
II.b.iii Magnetars 16
II.c. Black Holes 17
II.c.i. Active Galactic Nuclei 18
II.d. X-ray Binaries 19
II.d.i. Cataclysmic Variables 20
II.d.ii. Low Mass X-Ray Binaries 23
II.d.iii. High Mass X-Ray Binaries 23

III. DATA PROCESSING TREE 26

III.a. Method 28
III.a.i. Source Selection 28
III.a.ii. X-Ray Observations 30
III.a.iii. Multi-Wavelength Methods 32

IV. DATA 34

V. ANALYSIS 40

V.a. XSPEC Modelling 40
V.b. Color-Color Diagram 47
V.c. Multi-Wavelength Analysis 50

VI. CONCLUSION & FUTURE WORK 51

VI.a. K10 53
VI.b. M9 53
VI.c. E1 53
VI.d. K16 54
VI.e. E8 54
VI.f. I1 54
VI.g. D7 55
VI.h. Future Work 55

APPENDIX SECTION 57

WORKS CITED 79

LIST OF TABLES

Table **Page**

1. Summary of sources found in each observation. 34

2. List of interesting sources found in the 13 CXO observations. 39

3. Absorbed power law model fitting statistics for the bright sources........................... 43

4. Galactic column Density (absorption) for each source based on its RA and DEC. 43

5. Absorbed blackbody model fitting parameters and statistics. 45

6. Absorbed mekal model fitting parameters and statistics for source E8...................... 45

7. Absorbed apec model fitting parameters and statistics for source D7........................ 46

LIST OF FIGURES

Figure Page

1. A timeline of important dates in γ-ray astronomy. 2
2. Image of the galaxy taken by COS-B. 3
3. A pie chart representing the types of objects in the Fourth Fermi LAT Catalog. 4
4. Composite image of observations of the Crab Nebula in different wavelengths. 5
5. An 843 MHz radio image of the field of HESS J1616 from the Sydney University Molonglo Sky Survey. 7
6. Structure of an old, massive star. 10
7. The progenitor of a Type Ia SN 12
8. A sketch of the Crab pulsar's magnetosphere. 15
9. Artist depiction of a black hole with an accretion disk. 18
10. An example of the evolution of a CV form a pair of main sequence stars. 21
11. A possible evolution scenario for a HMXB/Be star from an initial binary system. 25
12. Schematic of how X-ray graze the telescope's mirrors to focus them on the detector. 26
13. The plot of 3FGL variability/curvature parameters that shows the clustering of pulsars along the bottom. 29
14. DS9 images of CXO observations 20324 (top left), 20325 (top right), 20326 (center), 23586 (bottom left) and 23587 (bottom right). 36
15. DS9 images of CXO observations 23588 (top left), 23589 (top right), 23590 (bottom left), and 23591 (bottom right). 37

16. DS9 images of CXO observations 23592 (top left), 23593 (top right), 23594 (bottom left), and 23595 (bottom right)... 38

17. Plots of K10, M9, E1, K16, E8, I1, and D7 (left to right, top to bottom) spectrums fitted with the absorbed power law model... 42

18. Spectrum plots with absorbed blackbody model fitted for sources M9(top left), E1 (top right), and I1(bottom center). 44

19. E8’s spectrum plotted with the absorbed mekal model fitted.................................. 45

20. Source D7's spectrum plotted with the absorbed apec model fitted. 46

21. Color-color plot of the Hard vs Soft X-ray colors for all 100 sources detected. 48

LIST OF ABBREVIATIONS

Abbreviation	Description
2MASS	Two Micron All Sky Survey
3FGL	3rd Fermi Gamma-ray LAT catalogue
4FGL	4th Fermi Gamma-ray LAT catalogue
a^*	The ratio of angular moment to maximum angular momentum
ACIS	Advanced CCD Imaging Spectrometer
AGN	Active Galactic Nuclei
Al	Aluminum
AMXP	Accreting Millisecond Pulsars
ARF	Auxiliary Response File
AXP	Anomalous Pulsars
BB	Blackbody
BH	Black Hole
BHC	Black Hole Candidate
BLR	Broad Line Region
c	The Speed of Light
C	Carbon
CALDB	Chandra Calibration Database

Abbreviation	Description
CCD	Charge-Coupled Device
CIAO	Chandra Interactive Analysis of Observations
CL	Chandrasekhar Limit
cm	Centimeters (10^{-2} meters)
COS-B	Cosmic Ray Satellite (Option 'B')
CSTAT	Chartered Statistician
CV	Cataclysmic Variable
CXO	Chandra X-Ray Observatory
DEC	Declination
DECaLS	Dark Energy Camera Legacy Survey
DECaPS	Dark Energy Camera Plane Survey
D.o.f	Degrees of Freedom
DSS2	2^{nd} Digital Sky Survey
ergs	a unit of energy
ESA	European Space Agency
EUV	Extreme Ultraviolet
eV	Electron Volt
Fe	Iron
FITS	Flexible Image Transport System

Abbreviation	**Description**
G	The Gravitational Constant
GAIA	Global Astrometric Interferometer for Astrophysics
GALEX	Galaxy Evolution Explorer
GeV	Giga-electron Volts (10^9 eV)
GLIMPSE360	Galactic Legacy Infrared Mid-Plane Surveys Extraordinaire
H	Hard X-ray Counts
H	Hydrogen
He	Helium
HEASARC	High Energy Astrophysics Science Archive Research Center
HESS	The High Energy Stereoscopic System
HETGS	High Energy Transmission Grating Spectrometer
HMXB	High Mass X-ray Binary
HR	Hardness Ratio
HRC	High Resolution Camera
IR	Infrared
IRAS	Infrared Astronomical Satellite
IRIS	Improved Reprocessing of the IRAS Survey
ISCO	Innermost Stable Circular Orbit

Abbreviation	**Description**
ISM	Interstellar Medium
J	Angular Momentum
J_{max}	Maximum Angular Momentum
keV	Kilo-electron Volts (10^3 eV)
kT	Temperature
LAT	Large Area Telescope
LETGS	Low Energy Transmission Grating Spectrometer
LMXB	Low Mass X-ray Binary
M	Medium X-ray Counts
M	Mass
$M_\odot$	Mass of the Sun (aka Solar Mass)
MeV	Mega-electron Volts (10^6 eV)
Mg	Magnesium
ML	Machine Learning
MS	Main Sequence Star
MW	Multi-wavelength
Myr	Million Years
NASA	National Aeronautics and Space Administration
Ne	Neon

Abbreviation	**Description**
nH	Hydrogen Column Density
Ni	Nickel
NIR	Near-Infrared
NLR	Narrow Line Region
Norm	Normalization
NS	Neutron Star
Null Hyp	Null Hypothesis
O	Oxygen
ObsID	Observation Identification
OSO-3	Third Orbiting Solar Observatory
P_{orb}	Orbital Period
PanSTARRS	Panoramic Survey Telescope and Rapid Response System
PWN	Pulsar Wind Nebula
PWR	Pulsar
QSO	Quasi-Stellar Object
R_{ISCO}	Radius of the Innermost Stable Circular Orbit
R_S	Schwarzschild Radius
RA	Right Ascension
RGB	Red Green Blue

Abbreviation	Description
RLO	Roche Lobe Overflow
RMF	Resonse Matrix File
S	Soft X-ray Counts
S	Sulfur
s	Seconds
SDSS	Sloan Digital Sky Survey
SGR	Soft-Gamma Repeaters
Si	Silicon
Signif	Significant Curvature
SMBH	Super Massive Black Hole
SN	Supernova
SNR	Supernova Remnant
STScI	Space Telescope Science Institute
TOPCAT	Tool for OPerations on Catalogues And Tables
UV	Ultraviolet
VTSS/Ha	Virginia Tech Spectal-Line Survey / Hydrogen alpha
WD	White Dwarf
WISE	Wide-field Infrared Survey Explorer
XMM	X-ray Multi Mirror

Abbreviation	**Description**
XRB	X-ray Binary
XRN	X-Ray Nova
yr	Year
α	Spectral Index
Γ	Photon Index
γ	Gamma
σ_{HR}	The error in the hardness ratio
χ^2	Chi-squared error statistic

ABSTRACT

The latest data release from the Fermi Gamma-Ray Space Telescope (the Fourth Fermi LAT Catalog) has more than 50% of the detected galactic sources yet to be identified. In an attempt to uncover the nature of some of these unknown sources, we observed thirteen sources within the galactic plane using the Chandra X-Ray Observatory (CXO). Analysis was performed using Chandra Interactive Analysis of Observations (CIAO) software in order to determine if any of these Fermi sources also emitted in the X-ray spectrum. We performed spectral analysis of seven X-ray sources, which had higher quality data. We also found fainter X-ray sources that lied within the Fermi radii and performed X-ray analysis on them. We also analyzed the available multi-wavelength data to shed light on the nature of these high energy sources.

I. INTRODUCTION

As technology improved, so too did the capabilities of γ-ray telescopes. While being able to detect higher energies allows us to see more objects, the amount of these high energy photons that reach the telescope are still very few. This is because γ-rays will annihilate or be absorbed and reemitted as lower energy photons if they interact with lower energy particles: something that the Universe is full of. To compensate for the lack of γ-rays reaching the telescopes, long exposures are needed for a source to be detected. This causes the resolution of γ-ray telescopes to be poor in comparison to those of even the next spectrum down, X- rays. Another cause of the low resolution of γ-ray observations is because the high energy photons cannot be bent or focused with mirrors like in other types of telescopes. The result is that γ-ray telescopes work similar to laboratory particle detectors: they detect a shower of particles from interaction with γ-rays and extrapolate the direction of the original γ-ray.

I.a. History of Gamma-ray Astronomy

γ-ray astronomy's directive is to study the Universe on a nuclear interaction and high energy level. After the detection of π-meson in 1947 along with the π-2γ decay, it was hypothesized that γ-rays could be produced by cosmic rays. This would allow us to see sources of cosmic rays such as supernovae and their remnants using γ-ray astronomy. However, because of the way γ-rays interact with low energy particles, they are absorbed in our atmosphere and space-based detectors are needed.

The first astrophysical γ-ray signal was detected by OSO-3 (Third Orbiting Solar Observatory) in 1968. The source of the signal was the galactic plane and gave insight into the instrumentational thresholds needed for detecting sources. Since then, we have built both detectors capable of detecting higher energy sources and detectors with better resolution as shown in the timeline of γ-ray detectors (Figure 1)

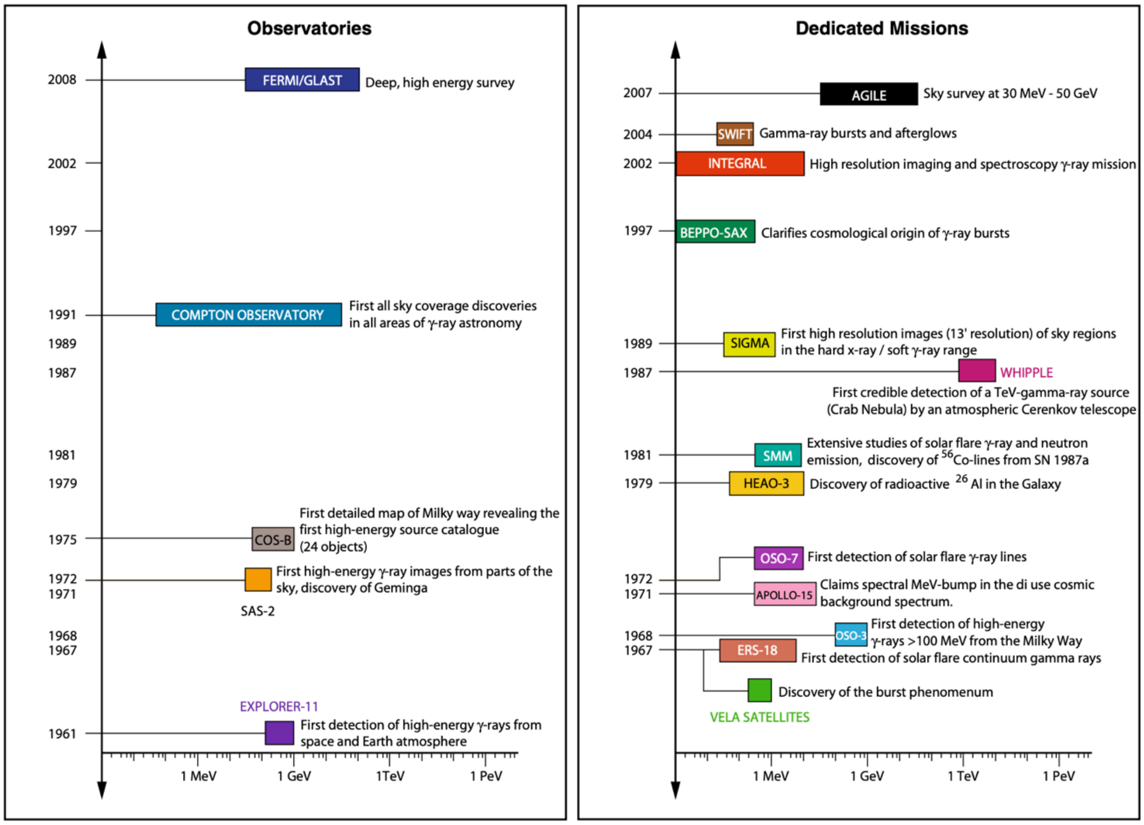

Figure 1: A timeline of important dates in γ-ray astronomy. (Pinkau 2009)

The launch of the first European Space Agency (ESA) mission to study γ-ray sources, COS-B, in 1975 showed just how important technology was to science as it quickly became the premier γ-ray detector of its era. With its capability of providing a large time integral, COS-B generated the first detailed map of the galaxy in γ-ray (Figure 2) and led to the discovery of the Crab and Vela pulsars in γ-rays.

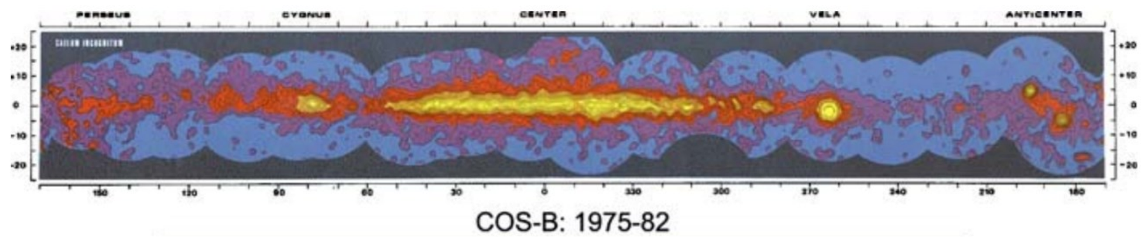

Figure 2: Image of the galaxy taken by COS-B. The Cygnus Region, Inner Galaxy, Vela Pulsar, and Crab and Geminga Sources beyond the "galactic hole" between 210° and 250° galactic longitude are visible. (Pinkau 2009)

As technology improved, we started to see γ-ray point sources embedded within the galactic plane, and also some located beyond our galaxy. To detect these sources, longer exposures were needed which lowered the resolution of these images. This makes pinpointing the exact location of the source very difficult and is a reason why so many sources are still unknown. With the latest release of data from the Fermi Telescope (the Fourth Fermi LAT Catalog), more than 28% (Abdollahi and al 2020) have yet to be categorized (see Figure 3). This percentage is even higher (>50%) among galactic γ-ray sources, which are the targets of this study.

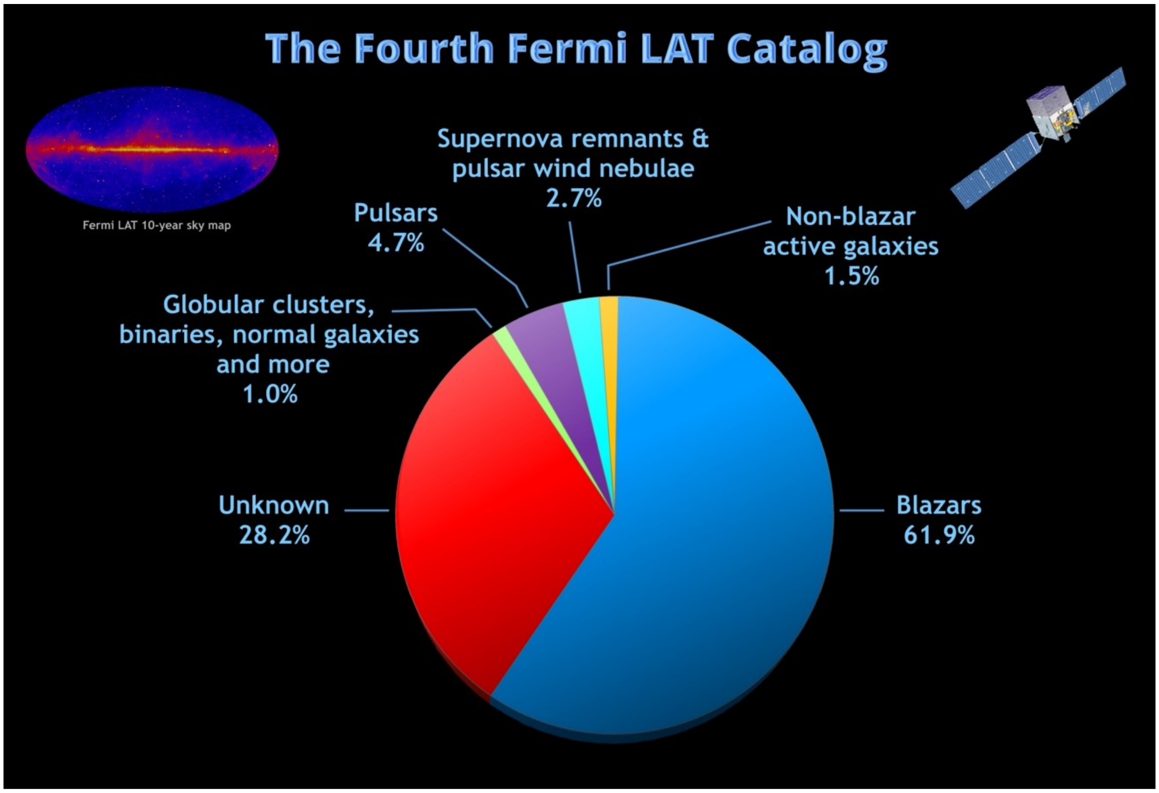

Figure 3: A pie chart representing the types of objects in the Fourth Fermi LAT Catalog. (Abdollahi and al 2020)

Types of γ-ray sources include pulsars (such as ones in the Crab and Vela nebulae), accreting binaries, accreting rapidly spinning black holes (which produce jets such as those considered active galactic nuclei (AGN), as well as supernovae and their remnants. Identifying these objects requires extensive knowledge in astronomy.

I.b. Why Multi-wavelength?

Using multi-wavelength analysis, we combine data from telescopes that operate in different spectra/wavelengths (γ-ray, X-ray, Ultraviolet (UV), Optical, Infrared (IR), Radio). This allows us to not only increase our accuracy in determining the location of a source, but also to accumulate more data in order to determine the nature of the source.

Astronomy first started with observations in the visible spectrum due to that being the only wavelengths we can see. As technology improved and we were able to observe the universe in other wavelengths, our knowledge of how stars and the universe evolved grew. Observing in one wavelength is like looking at only one piece of the puzzle. As you can see in Figure 4, the images of the Crab nebula in different spectra all look different and tell us something about the object.

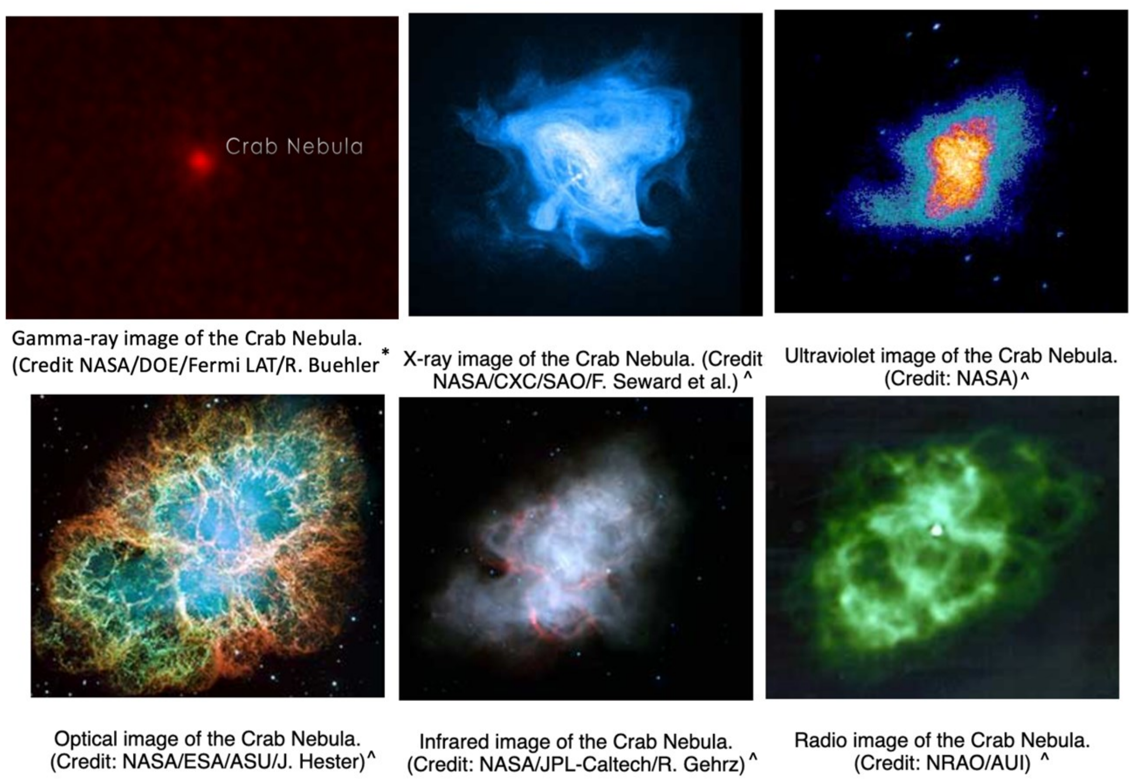

*Figure 4: Composite image of observations of the Crab Nebula in different wavelengths. ^ from (The Imagine Team at NASA Goddard Space Flight Center 2013). * from (NASA Goddardd Space Flight Center 2016)*

If we just look the γ-ray picture (top left in Figure 4), the Crab Nebula looks like a red blob. However, by moving down the electromagnetic spectrum to X-rays (top middle), we can see that there is a central star that is pulsating X-rays due to the jet and its rotation. Moving to UV (top right), we see that the nebula appears even bigger than it does in the X-ray or γ-ray spectrum. This is due to the electrons responsible for emissions in the UV being farther away from the central pulsar. And because they are farther way they are not as energetic and "hot" as the electrons closer and emitting in the X-ray spectrum. The bottom left panel in Figure 4, shows the Crab Nebula in visible light as we can see it with an optical telescope, more specifically the Hubble Space Telescope. In this spectrum we can see red fringes from the precursor star. Conducting spectroscopic analysis on this, we can figure out the elements that make up the nebula and categorize the precursor star. By taking multiple images over long periods of time, we can measure the movement of the filaments, trace them back to their origin and calculate when the supernova occurred. Finally, looking into the radio image (bottom right), we can see that the central pulsar also emits in the radio wavelength. This allows further categorization on the type of pulsar and the type of precursor star that led to this nebula. These are all basic conclusions from these different observations and so much more can be learned by more complicated analysis of the data in each spectrum.

Multi-wavelength observations are needed to build the complete story. For instance, the angular resolution of the Fermi γ-Ray Large Area Telescope (Fermi LAT) is < 3.5° in 100 MeV band, < 0.6° in 1 GeV band and < 0.15° when observing in the bands above 10 GeV (Atwood, et al. 2009). Compared with Chandra X-Ray Observatory's resolution of 0.5" (Weisskopf, et al. 2002) and the Hubble Space Telescope's resolution of 0.05" in the optical/NIR wavelengths (note: " represents the unit arcseconds with $1'' = \frac{1}{3600}$ of a degree). To visualize this, look at Figure 5. The cyan circle represents the 90%

certainty radius of the γ-ray source detected with Fermi, while the green boxes with cross sections represent entire observing fields using Chandra. Using multi-wavelength analysis like this essentially lets us "zoom-in" on the source to see what object is emitting the γ-rays.

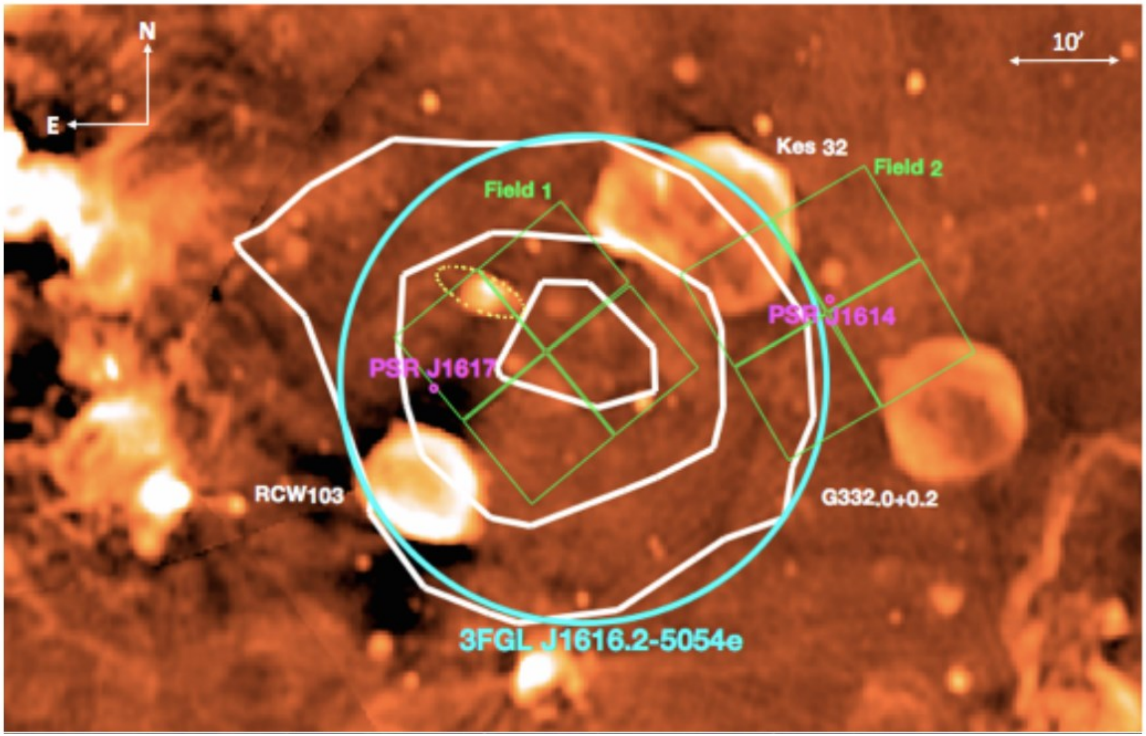

Figure 5: An 843 MHz radio image of the field of HESS J1616 from the Sydney University Molonglo Sky Survey (Mauch, et al. 2003).. The ACIS-I fields of view from the CXO observations are shown in green, the HESS J1616 contours are shown in white, the extent of the Fermi-LAT source 3FGL 1616.2–5054e is shown in cyan, and the two known pulsars in this field are shown in magenta. (Hare, et al. 2017)

While it is sometimes possible to jump from γ-ray observations directly to visible, there are two very important reasons why stepping down to X-rays first is necessary. The first being the nature of γ-ray sources: because both γ-rays and X-rays are such high energy, sources that emit in the γ energy spectrum will most likely also emit in the X-ray. It is not guaranteed that a γ-ray source will emit in the optical or IR. The second reason is the large uncertainty in the locations of γ-ray sources (shown as large ellipses; cyan circle in Figure 5). If an optical observation of a γ-ray source was done, there would be thousands of optical sources that could correspond to the location of the γ-ray source. It would be near impossible to determine which of these was the origin of the γ-rays, thus impossible to do multi-wavelength analysis and determine the nature of the γ-ray source. These reasons were the driving factors to the development of the Chandra mission: first collect X-ray data and determine X-ray source locations to narrow down the regions to look for potential optical or even IR sources.

II. TYPES OF X-RAY OBJECTS (Seward and Charles 2010)

To understand how X-rays are emitted from stellar objects, it is crucial to understand the evolutionary process of stars. It is important to note that the speed of evolution, that is how long it takes a star to evolve into and end-life form, is highly dependent on its mass/size. Under immense pressure and temperature, stars "burn" hydrogen in their core, fusing ^1H atoms together to form ^4He. As the mass increases it contracts the core, turning gravitational potential energy into thermal energy and burns even more hydrogen. When the core runs out of hydrogen to turn into helium, the star enters its red giant phase. During this part of its life, the star's core now mostly helium, contracts, while the outer layer expands. This heats up the outer hydrogen layer until it reaches the temperature needed to begin fusing hydrogen into helium again. Meanwhile, in the core, the contraction increases the temperature enough to fuse ^4He into ^{12}C (and some ^{16}O). When the core runs out of helium to fuse, the end-life process splits into two possible scenarios.

If a star has less than ~$8M_{\odot}$, then its core collapses and burns more helium. This raises the temperature until the point which electron degeneracy pressure takes over for the fusion pressure and temperature stops increasing. This stops fusion and the star's outer layers then expand until they are blown off and dispersed, leaving behind its carbon and oxygen core. The star has become a white dwarf (WD) and maintains its shape via electron degeneracy pressure. That is, the pressure from the electrons refusing to occupy the same state (Pauli exclusion principle), and it is what keeps stars from collapsing under their own gravity.

If the mass of the star is greater than ~$8M_{\odot}$, then the core contraction increases the temperature enough to begin fusing ^{12}C and ^{16}O into ^{20}Ne and ^{24}Mg while the outer layers again expand. This process of the core contracting when out of fuel repeats for ^{20}Ne and ^{24}Mg into ^{28}Si and then for ^{28}Si into ^{52}Fe and ^{56}Ni. This process creates an onion like structure of layers that consists of different elements (as depicted in Figure 6).

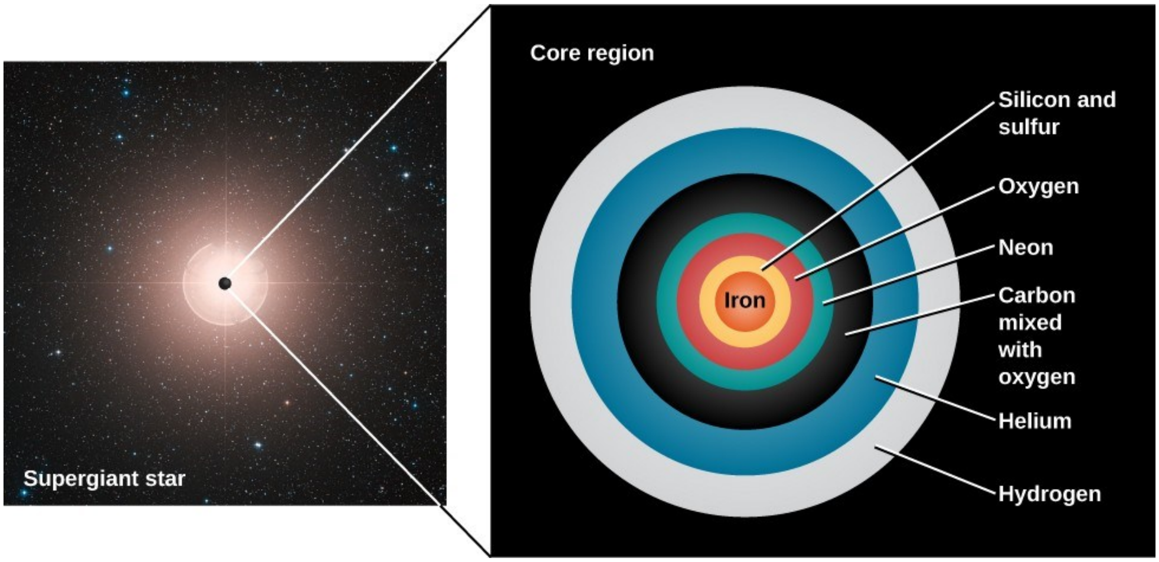

Figure 6: Structure of an old, massive star. Right before going supernova, the massive star has many layers of elements that resemble an onion. Note that the layers are not to scale. (Image credit: modification of work by ESO, Digitized Sky Survey) (Lumen Learning n.d.).

Note that main sequence stars maintain their shape and size by the pressure generated from the immense heat. The outward heat pressure counteracts the gravitational force inward. When the core of the star is iron, the star can no longer fuse it into heavier elements and generate enough heat to maintain its shape. The only thing left to do now that the star has ran out of fuel is to go supernova (SN) and leave behind its core as a neutron star (NS) or a black hole (BH). The core's mass determines its final stage: if the mass is greater than $\sim 3M_\odot$ (referred to as the Oppenheimer Volkov limit) then it becomes a BH, otherwise it is a NS.

II.a. Supernovae and Supernova Remnants

Supernovae are the most energetic stellar events known, having energies $\sim 10^{51} ergs$. Most of this is initially energy of motion and released during the "explosion". There are two main types of SN: Type Ia and Type II. Type Ia SN are from binary white dwarf (WD) systems. Consider a two-star system. The more massive of the two will evolve first. As its “red giant” layer expands, it fills up the Roche Lobe of the second star. A Roche Lobe is the point in a binary system where the gravitational pull switches from one star to the other. The second star then starts to accrete, or steal, the mass of the first star, eventually becoming more massive than the first star. This leaves the first star with less than $1.44\ M_{\odot}$ (the Chandrasekhar limit (CL)). Because the first star has less than the CL of mass, it becomes a WD. The 2nd star rapidly begins to evolve, having its “red giant” layer now fill up the Roche Lobe of the WD and it now begins to accrete mass until it surpasses the CL. At this point the WD collapses under its own gravity leading to nuclear detonation of its core, which we see as the Type Ia Supernova.

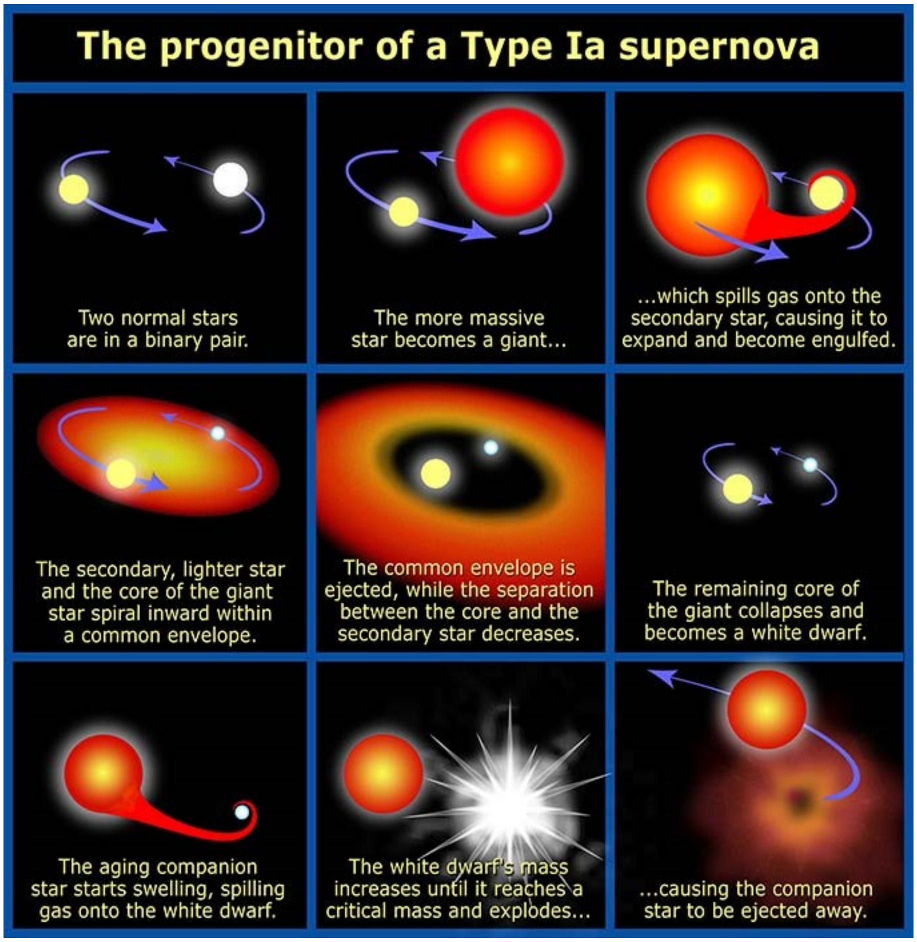

Figure 7: The progenitor of a Type Ia SN (illustration credit: NASA, ESA, A. Field (STScI)) (NASA 2004).

Type II SN are from the gravitational collapse of massive stars (mass $> 8M_{\odot}$). As iron is continually produced, increasing the mass of the core. As the mass increase, so does its temperature until it reaches the point when iron can decompose. When this happens, energy is absorbed, decreasing the pressure and the core shrinks until stabilized by electron degeneracy pressure. The free protons created from the decomposition of iron merge with free electrons to form neutron and neutrinos. Fewer free electrons mean there is less electron degeneracy pressure and the core shrinks again. The process repeats until gravity overcomes the degeneracy pressure at which point the core collapses into a neutron star (NS) sending a shockwave that ripples through the layers, expelling them outward. The light from this is the Type II SN.

As the material ejected (ejecta) expands, it runs into the surrounding material, heating it up to extremely hot temperatures and generating X-rays. X-rays from SN could also be emitted from γ-rays, generated by the short-lived nuclei, being Compton scattered into the X-ray waveband. If a neutron star (NS) forms from the SN, the NS itself will emit X-rays that could be detectable if it is close enough to us. In the early life of the NS, it could be obscured from direct observation by the surrounding gas of the SN and thus would most likely be categorized as a supernova remnant (SNR).

SNRs have three phases of evolution. The first phase, called free expansion, is when the shell of ejecta expands and gathers the surrounding medium until the mass of the coalesced material is equal to the original mass of the ejecta. Next comes the blast wave phase, sometimes referred to as the Sedov-Taylor phase. During this phase, the collected material's mass is greater than the ejecta's. This creates a barrier that is increasingly difficult to traverse and ends up generating two shockwaves. One of these continues to move out while the other moves inward and between them the temperature is hot enough to emit X-rays. Lastly, the phase that is mostly radiation: as the ejecta continues to expand, it cools until it is indistinguishable from the surrounding medium. There are four classifications, at least in regard to X-rays: shell-like, filled center, composite, and missed morphology. Shell-like have bright radio and X-ray emission from the limbs of the SNR, while the filled center category has the radio and X-rays bright in the center and are absent (or are weak) in the limbs. Composite is a combination of these two previous categories and the mixed morphology is shell-like in the radio spectrum but filled-center in the X-ray.

II.b. Neutron Stars

Neutron stars (NS) are created from type II (and sometimes type 1b/1c) supernovae if the mass of the stellar core is ~ 2 $M_{\odot}$. This is the theoretical maximum mass, although the majority of observed NS are around 1.4 $M_{\odot}$. They are characterized as having a radius that is ~12km, making them incredibly dense (second only to black holes). This density leads to a strong gravitational field. They also exhibit strong magnetic fields that act as a dipole. The magnetic field is left over from the progenitor star and gets compressed/concentrated by gravitational collapse. NS are very hot, with initial temperatures $\sim 10^{11} K$ but cool rapidly from neutrino emissions. When the temperature cools down to $\sim 10^{6} K$, after about 100 years post-SN, the blackbody radiation is within the X-ray band. The X-rays are from lighter elements in the NS's atmosphere (only ~1cm thick) that accumulate via accretion or colliding with the interstellar medium (ISM). At this age, the young NS can be differentiated from the SNR in observations. In fact, most young NS emit pulsed X-ray radiation thermally (from the surface) and non-thermally (from the magnetosphere). We refer to these NS as pulsars and are explained in more detail below. At around 10,000 years post-SN, the NS has cooled enough to emit photons in the optical band. However, they usually appear dim despite their high temperatures due to their size. During the collapse of the progenitor star, angular momentum must be conserved, resulting in NS having very high spin rates. They eventually spin less and less due to emitting energy and conservation of energy.

II.b.i. Pulsars

As stated above, Pulsars are NS that emit pulsed radiation. Radio waves are created through synchrotron radiation when electrons stop rotating with the NS and crosses magnetic field lines. High energy pulses could be from the magnetic poles or the outer gap, a region between the last open field lines and the null-charge surface. At the magnetic poles, the emission is caused by pair production close to the surface and for the outer gap, radiating particles come from pair cascade. Figure 8 shows a sketch of a pulsar.

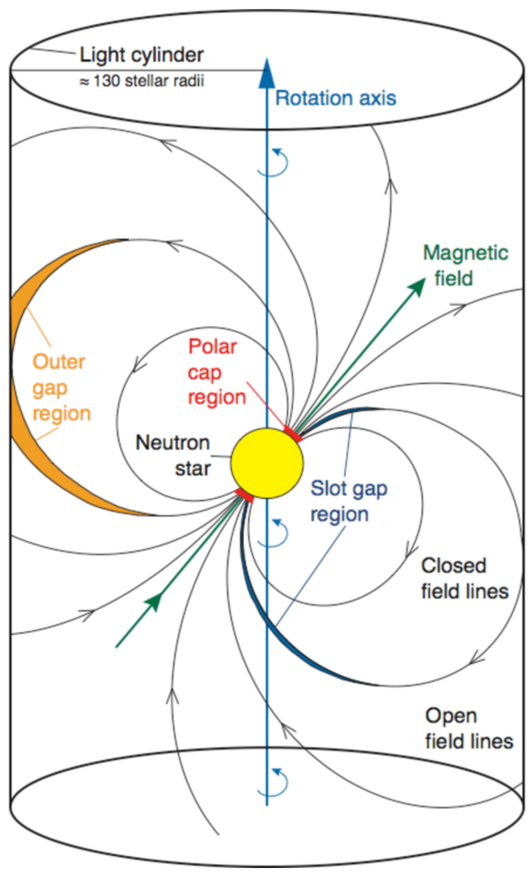

Figure 8: A sketch of the Crab pulsar's magnetosphere. The shaded regions are vacuum gaps or vacuum regions. These are plasma filled regions with low enough density to allow electron to be accelerated to very high energies (Aliu, et al. 2008) .

In both cases, photons are generated via the inverse-Compton process or curvature radiation. Both the outer gap and the magnetic field rotate with the NS but can be misaligned with the axis of rotation. This misalignment causes the lighthouse effect and is why we see periodic pulses from the NS. We could even not see any pulse if the beam of radiation from the magnetic poles doesn't cross our line of sight. The pulsar can still be indirectly observed by analyzing the surrounding nebula.

II.b.ii. *Pulsar Wind Nebulae*

A Pulsar Wind Nebula (PWN) is a cloud of electrons and positrons and has a magnetic field between $10^{-5} - 10^{-3}\ G$. They are the most dominant feature in most X-ray observations and all fast pulsars with strong magnetic fields are surrounded by them. The radiation is due to electrons interacting with the magnetic field, producing synchrotron radiation with a power law spectrum: $N = k(h\nu)^{\alpha}$ (note that when referencing the power law spectrum model's photon index: $\Gamma = \alpha + 1$). The particles and field flow from the NS and pass through a shock that accelerates the particles into the power law spectrum and the electron velocities are then oriented randomly. This gives the PWN the property of radiating isotropically and allows it to be visible even if the NS isn't. Because the particles lose energy after passing through the shock, radio observations show a larger PWN than in X-ray. The relation between the NS and the PWN allow us to determine the output of the NS by the strength of the PWN emissions. Also, because synchrotron luminosity is proportional to the magnetic field, bright PWN are synonymous with strong magnetic fields. Some pulsars can be ejected, leaving behind the PWN and creating a new one as it moves through space.

II.b.iii. *Magnetars*

Some pulsars that have been found have periodic X-ray emission that is too long to be associated with young NS (~5-12s) and high spindown rates. High spindown rates imply energy rates to be too low to account for the steady luminosity of these objects ($L_X \approx 10^{35} - 10^{36}\,\frac{ergs}{s}$). From calculations, it is seen that these objects have incredibly strong magnetic fields ($10^{14} - 10^{15}\ G$) at the poles. The strong magnetic field can then heat the crust of the NS to account for the observed luminosity. It can also occasionally generate cracks in the crust that releases bursts of high energy in the soft γ-ray/hard X-ray bands. These objects are known as anomalous pulsars (AXP) or soft-γ repeaters (SGR). But when the magnetic field can be calculated and is shown to be of the high magnitudes described, we call them magnetars.

II.c. Black Holes

Black holes interact with other stars in a unique way due to their own unique properties. Black holes are massive compact objects that curve space-time so much that any light emitted by the object can never escape. They are characterized by their Schwarzschild radius (R_S), which is the region around the black holes that the escape velocity is equal to the speed of light. However, stellar sized BH are also described by their spin. For a BH of mass M, the maximum angular momentum it can have is described as $J_{max} = \frac{GM^2}{c}$ where G is the gravitational constant and c is the speed of light. The angular momentum (J) of the BH, is estimated from the temperature of the accreting material. It is the ratio $a^* = \frac{J}{J_{max}}$, which can range from -1 to 1, that we use to describe the spin of the black hole. If $a^* < 0$, the BH is spinning in the opposite direction of the binary's rotation. A value of $a^* = 0$ corresponds to a non-spinning BH and is referred to as a Schwarzschild BH. When $a^* = 1$, the BH is spinning at its maximum speed and we refer to these as Kerr BH.

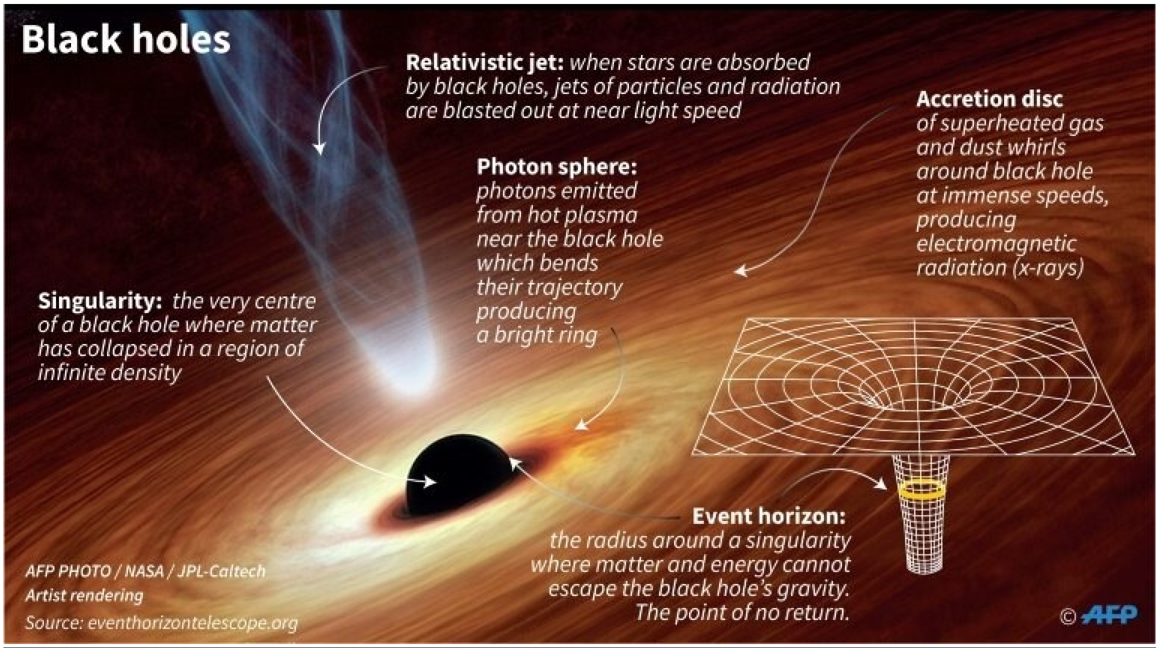

Figure 9: Artist depiction of a black hole with an accretion disk. In the bottom right corner, depiction of the distorted space-time fabric due to a black hole and shows the event horizon. Image credit: AFP PHOTO/NASA/JPL-Caltech/eventhorizontelescope.org (Coustal 2019)

II.c.i. Active Galactic Nuclei

Spiral galaxies that have very bright nuclei, referred to as Seyfert galaxies or active galactic nuclei (AGN), have been discovered to have super massive black holes (SMBH) at their center. Just like in quasi-stellar objects (QSO), an AGN accretes material on the accretion disc, which due to friction heats up and emits light across the electromagnetic spectrum al lthe way up to X-rays. In fact, if the AGN was so far away that we couldn't resolve the host galaxy, then we would classify it as a QSO. Just like QSOs, AGN produce jets of from its poles. These are generated by the synchrotron radiation of relativistic electrons spiraling in the tightly wound magnetic field of the SMBH. Because the jets are hottest near the core of the AGN (near the SMBH), they can be observed in the X-ray spectrum. As the jets move farther away, they cool down when they interact with the surrounding gas and eventually, they terminate. When the jets are cool enough, they are observable in the radio band. AGNs can also be classified into several types, two of the main ones being dependent on the AGN's orientation toward us the observers. Seyfert 1 galaxies are AGN that have high inclination and the emitted broad line region (BLR) can be observed. If the inclination is too low, the torus surrounding the AGN obscures the BLR and only the narrow line region (NLR) is detected. These are referred to as Seyfert 2 galaxies, have lower X-ray luminosities, and absorption columns (due to the emitted photons passing through the torus). Due to the brightness of AGN, they can be observed across multiple spectrums and can be fit with a power law model with spectral index of $\alpha \sim 1$. The synchrotron radiation emitting jets dominate in the radio, while the thick torus emits in the mid- and far-IR. The accretion disk is responsible for the "blue bump" in the optical and UV. X-rays and sometimes γ-rays are emitted via inverse-Compton scattering of the photons from the disk by high energy electrons. Some AGN also have outflowing winds that drive matter off the disk and areas surrounding the core. These winds produce emission lines in the spectrum. Also, in Seyfert 2 galaxies, the spectra can be well represented by a hard X-ray power law with slope of -0.7.

II.d. X-Ray Binaries

So far we've discussed how lone stellar objects can emit X-rays. But what about when a stellar object exists in a binary system? From sky surveys, we have come to realize that there are only a few hundred luminous X-ray binaries (XRB) within our galaxy. This is opposite of what is expected due to about half of all the stars in our galaxy are in binary systems. This must mean that the formation of XRB requires very specific circumstances. We also have come to realize that the location of the "two" types of XRB is dependent on their makeup. High mass X-ray binaries (HMXB) are found in or near star forming regions where younger stars are found. While low mass X-ray binaries (LMXB) are found in places where old stars are, notably near the galactic center.

The compact objects in HMXB and LMXB can be black holes, NS or WD. To determine if a BH is the compact object in a binary, the mass of the compact object must be determined. In a HMXB system, this is done by optical observations of the donor star when the compact object is in quiescence, or for more accurate mass calculation, when the compact object is eclipsed by the donor. In LMXB systems, good black hole candidates (BHC) exist in soft X-ray transients, also known as X-ray Nova (XRN). In this case, the spectrum is needed to determine if the compact object is a NS or a BH. NS have two thermal (blackbody) components: one from the NS and one from the disk. BH spectra usually display a power-law component at high energies and a thermal (blackbody) component from the disk at low energies. When the accretion disk forms around a BH, it's inner radius reaches a point, before the event horizon, that the material starts to rapidly spiral toward the BH. This is called the innermost stable circular orbit (ISCO) and varies based on the spin of the BH. For Schwarzschild BH, $R_{ISCO} = 3R_S$, while for Kerr BH, $R_{ISCO} = 0.5R_S$.

Now that we've discussed how to determine if a BH is part of the binary system, lets discuss the ones involving NS and WDs. Starting with the lowest mass binaries then working up to the higher ones, brings us to what are called cataclysmic variables.

II.d.i. Cataclysmic Variables

Cataclysmic Variables (CVs) are interacting binaries that have a WD as its compact object interacting with low mass companion. They evolve from two main sequence stars. The first star to evolve has its red giant phase engulf the other star. The main sequence star then spirals in toward the core of the evolved star creating a short period binary. This expels the red giant envelope, leaving behind the core of the evolved star as a WD. As the main sequence star evolves into a cool late-in-life star, the WD will accrete matter from it. This accretion leads to continuing, irregular eruptions (nova or dwarf nova) which is what gave these objects to cataclysmic designation.

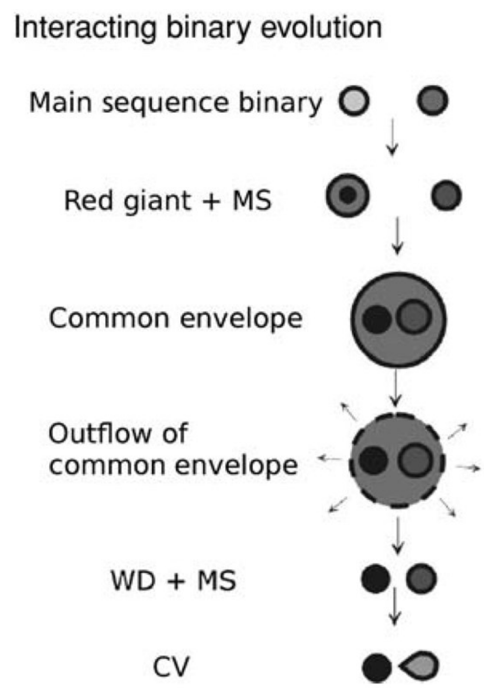

Figure 10: An example of the evolution of a CV form a pair of main sequence stars. (Seward and Charles 2010)

As the matter is transferred from the companion to the accretion disk and from the disk to the WD, it heats up. Half of the total accretion luminosity is deposited on the disk, this along with the faint companion is why most of the visible light is from the accretion disk. The other half is released into the boundary between the disk and the WD, bringing accretion to a stop. This region is even hotter and emits in the extreme ultraviolet (EUV) and soft X-ray.

They are abundant in our galaxy due to low interstellar extinction. They also have well defined orbital mechanics which makes them ideal for studying the physics of accretion onto compact objects.

CVs can be split up into 2 categories, magnetic and non-magnetic. CVs with a magnetic field powerful enough to overtake the accretion flow are called Magnetic CVs. These can then split into two categories: polars and intermediate polars. Polars have such a strong magnetic field that it causes the WD's rotation to be locked with the orbital period and no accretion disk is formed. Instead, matter is threaded down to the surface of the WD near its poles along the magnetic field lines. The matter hits a shock above the surface which turns the kinetic energy into thermal energy and generating hard X-rays. The hard X-rays heat up the WD surface which leads to blackbody radiation as soft X-rays. The electrons spiraling in the magnetic field produce synchrotron radiation in the optical and IR energies. Intermediate polars have a truncated accretion disk with the inner disk being replaced with the magnetic field, like in polars. Because the WD's spin is not locked with the orbit, X-ray emission is seen as pulses in the ~30s-1hr range and have a hard X-ray spectrum. The X-ray spectrum from CVs also falls into 2 categories (mostly aligned with the magnetic or non-magnetic designation). First, the spectra have strong H- and He-like emission lines of O, Ne, Mg, Al, Si and S, as well as the entire Fe L complex from ions XVII-XXIV. The spectra can be well fitted with a multiple temperature plasma then a cooling flow model and are mostly associated with non-magnetic CVs. The other is when the spectra have a strong, hard power law component and the emission lines are not well fitted with a cooling flow model as only the Fe XVII line shows up. This means that a photoionization model is needed and are usually created by magnetic CVs.

II.d.ii. *Low Mass X-Ray Binaries*

LMXB consist of a compact object and an old star ($\lesssim 1M_{\odot}$) where the material from this old star fills the Roche Lobe and accretes onto the compact object. The material forms an accretion disk and then falls onto the compact object, generating X-rays. The nature of the compact object can be inferred in a few different ways. If the LMXB is a weak source and nearby, then the compact object is a WD. If X-ray bursts or pulsations are observed, then the compact object is a NS. Lastly, the compact object is a black hole if the LMXB is luminous and has a soft X-ray spectrum. If the inclination of the disk is too high, the compact object will be obscured from view and can only be detected through the hot, X-ray emitting corona that expands above the disk. The donor star being so faint, it can only be observed in the IR when it eclipses the compact object, also creating dips in the X-rays detected. X-rays burst can be generated in two ways, the first, called Type I, are due to a build up of hydrogen on the surface of the NS. The hydrogen quickly fuses into He and then He into C, creating the flash. This is seen as blackbody radiation. The brightest type I bursts can also temporarily increase the radius of the NS. The other, Type II, is due to the weak magnetic field: as matter accumulates on the magnetic field, it becomes too heavy and breaks through creating less energetic and rapid bursts. As stated before, the accretion process increases the spin of the NS and they can reach 1ms rotation periods. We refer to these as accreting millisecond pulsars (AMXP) and they are potential gravitational wave generators.

II.d.iii. *High Mass X-Ray Binaries*

HMXB consist of a compact object and a massive young star (an O or B type stars), hence why they are usually found in regions where stars are formed. Young stars lose mass through their strong stellar winds at a rate of $10^{-5} - 10^{-4} \frac{M_{\odot}}{yr}$. About 0.1% of this ends up captured by the NS and provides a significant fraction of the seen X-ray luminosity, the rest being likely from the filling of the Roche Lobe. The wind ends up in an accretion disk and is guided to the NS's poles by its magnetic field. The accretion of material causes the NS to spin-up and can be seen as an increase in its luminosity. If the disk or wind is inhomogeneous, periods of quiescence can happen and the NS spins down. When the wind is dense and not highly ionized, the elements in the wind can absorb the energy from the emitted X-rays, thus obscuring the soft (low energy) X-rays. This is observed in the spectrum and characterized as a change in the column density of material between us and the source. However, if the NS is bright enough, it will ionize the wind and thus the spectrum is not affected. HMXB can be categorized in two groups: (1) ones that involve OB supergiant stars and (2) ones that involve mid-B or main sequence primaries. The first of these groups correspond to only 11% of HMXB. These yield a relationship which is roughly constant with orbital period and expected density variability of wind. The second is characterized by a weak wind. Instead, Be stars spin so fast that their material forms an equatorial disk which the NS passes through and X-rays are generated with long orbital periods and long periods of quiescence. The hard X-rays generated by the accreting NS will interact with the stellar wind, being scattered, absorbed and reprocessed. This results in an X-ray spectrum that is continuous and has emission lines that correspond to the elements in the wind. If the column density is low, the continuum dominates, and the emission lines are weak. Compton scattering of the X-rays can also create a shoulder on the emission lines due to the expansion of the stellar wind.

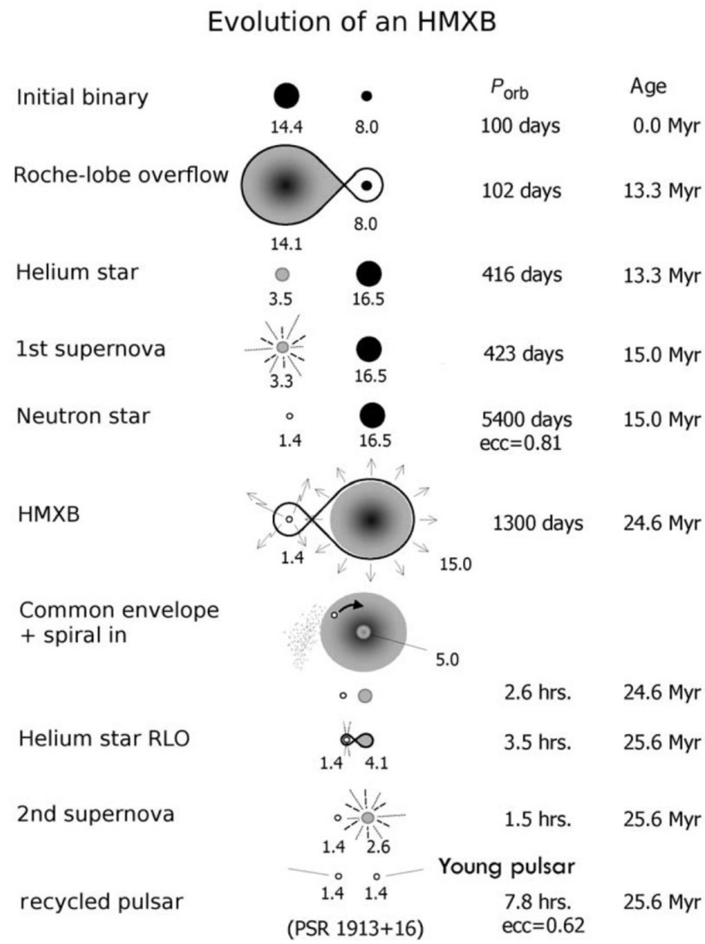

Figure 11: A possible evolution scenario for a HMXB/Be star from an initial binary system. In this binary system, one star is much more massive than the other and evolves first. The time and period stated are approximations. Image based on Tauris & van den Heuvel,2006. (Seward and Charles 2010)

III. DATA PROCESSING TREE

Unlike Optical and IR telescopes where the main data is in the form of an image, both γ- and X-ray telescopes generate data as event files. These files can be thought of as a 4-dimensional array with each dimension representing the following: was a photon detected (yes or no), the time it was detected, the location on the detector the photon hit, and the energy of the photon. Because of the high energy nature of X-rays are collected (observed) on the detector by being reflected off mirrors. However, an X-ray can only be reflected if its angle of incidence is very small, with an efficiency of 1 when the angle of incidence is < 1°. This is precisely how the Chandra X-ray Observatory (CXO) works as shown in Figure 12.

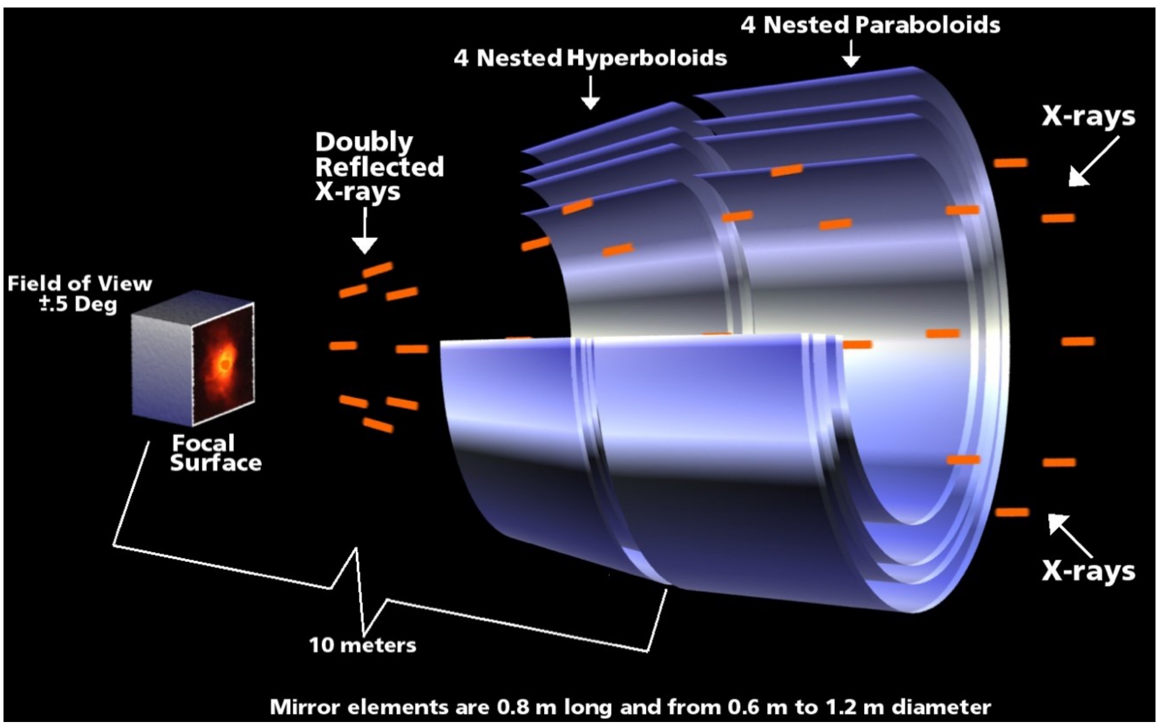

Figure 12: Schematic of how X-ray graze the telescope's mirrors to focus them on the detector. Illustration: NASA/CXC/D. Berry. (Harvard-Smithsonian Center for Astrophysics 2012)

The focused X-rays in CXO will hit either the High Resolution Camera (HRC) or the Advanced CCD Imaging Spectrometer (ACIS) depending on the observational setup.

CXO also has two high resolution spectroscopy instruments: the High Energy Transmission Grating Spectrometer (HETGS) and the Low Energy Transmission Grating Spectrometer (LETGS). These work by being deployed behind the mirrors to pass the X-rays through a gold diffraction grating. But because they interrupt the focusing of the X-rays on the HRC or ACIS, longer exposures are needed to use them in conjunction with HRC or ACIS (Harvard-Smithsonian Center for Astrophysics 2019). Whichever instrument on Chandra one chooses, the limitations to the data collected requires data processing and analyzing to extract information and determine the nature of the source(s) observed. Even then, X-ray photons/flux alone isn't sufficient enough to determine the nature of an object. Thus the need for multi-wavelength analysis. For example, XRBs need observations in other wavelengths to find the companion of the X-ray source for proper classification.

Most of the tools needed to process and analyze the observation data are provided to the public by each detector. Making the tools available to the public allows cross-mission analysis to be standardized. Chandra Interactive Analysis of Observations (CIAO)[1] is the software designed by the Chandra X-Ray Center for analyzing data generated by the Chandra X-ray Observatory (CXO) and has many data processing pipeline threads available to follow depending on the type of research being conducted. More detail about all the software and tools described below can be found in Appendix A.

[1] https://cxc.harvard.edu/ciao/

III.a. <u>Method</u>

III.a.i. Source Selection

The initial inspiration for this project was to find pulsars within our galaxy. Based on the 3FGL and 4FGL (the Third and Fourth Fermi LAT catalogs), plots were made based on: (1) the variability of the data over the catalog's observations and (2) the deviation of the source's spectrum from a power-law (curvature in Figure 13). In this plot, known pulsars are congregated in a region defined by variability less than 70. We then narrowed our selection criteria down to curvature > 5 and variability < 50. These chosen to minimize the unknown Fermi sources while still being within the area that correlates to pulsars. Essentially, trying to maximize the chances that the Fermi source is in fact a pulsar.

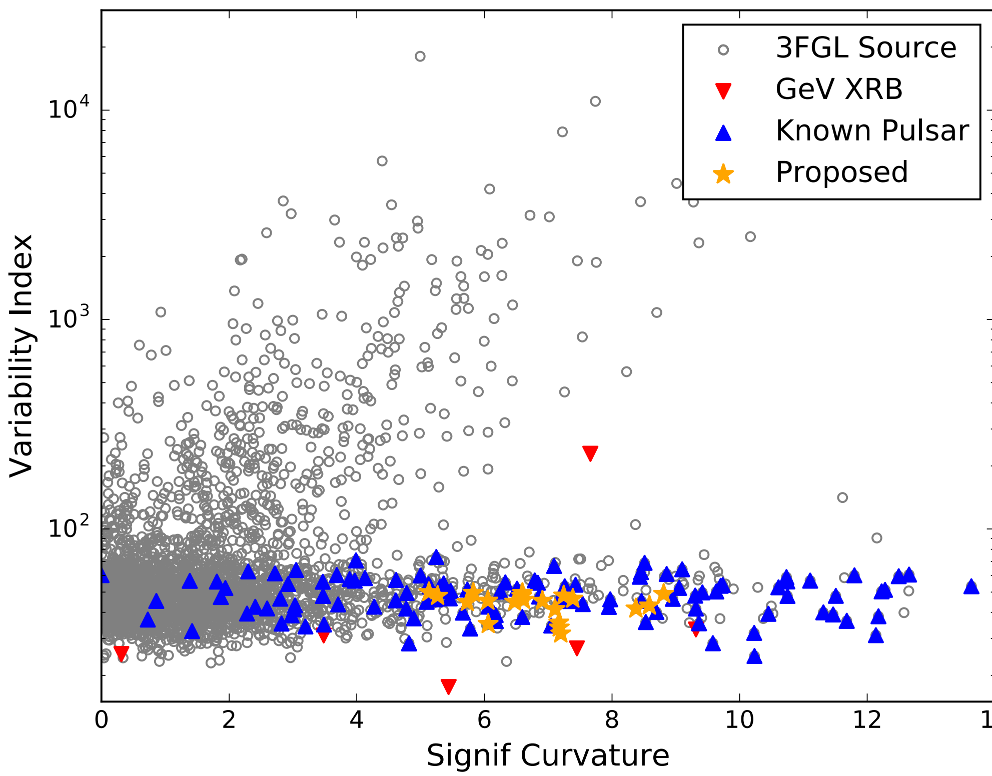

Figure 13: The plot of 3FGL variability/curvature parameters that shows the clustering of pulsars along the bottom. The shaded rectangle (bottom right) indicates the chosen parameter criteria for maximizing the ratio of pulsars to unknown sources. The yellow stars indicate proposed sources, 13 of these were approved and are the sources we analyzed.

The sources we wanted to look further into were chosen from the yet to be classified sources that also inhabited this carefully selected parameter space. Due to the similarity between pulsars and AGN, it is possible for our selected Fermi sources to include them. However, only ~0.5% of the 3FGL sources in this parameter space were found to be AGN. To decrease the probability even further, the list of potential sources was then finalized by picking those that are within the galactic plane ($|b| < 3.5°$; sources shown in Figure 13 as yellow stars). This resulted in 13 observations being selected to observe in the X-ray.

III.a.ii. X-Ray Observations

The thirteen Fermi sources chosen were observed by the CXO's advanced CCD imaging spectrometer (ACIS) and observation IDs (obsids) 20324-20326 and 23586-23595. More specifically, the observations utilized the ACIS-I chips, the detector was operated in VFAINT mode for an exposure time of $10ks$. Once each CXO observation was made, the data was processed using CIAO version 4.13. For this project, we wanted to determine the counts and fluxes of sources in my observations then extract the spectrum of the sources for model fitting. To do this, we first followed the "Calculate source count rates and flux[2]" pipeline. After downloading the data from Chandra, the data was reprocessed using *chandra_repro*[3] to ensure proper instrument noise was removed. Next, the *fluximage*[4] tool was used with the following set parameters: bands=csc,broad (to extrapolate the data in the soft ($0.5 - 1.2\ keV$), medium ($1.2 - 2.0\ keV$), hard ($2.0 - 7.0\ keV$) and broad ($0.5 - 7.0\ keV$) X-ray energies), bin=1 (so each pixel corresponds to 0.5 arcsec), and psfecf=0.9. *Wavdetect*[5] was used to find the X-Ray point sources and generate a list with their coordinates. The scales used were 1, 2, 4, 8, 16, and 32, along with the broad psfmap and expmap files for each observation. From here, source and background files were made using the *roi*[6] tool then merged into a single file for each observation using *splitroi*. When running *roi*, the parameter group was set to 'exclude' so that if detected sources were touching, then a target source would exclude the source touching it. For example: if source A was touching source B and source B was touching

[2] https://cxc.cfa.harvard.edu/ciao/threads/fluxes/index.html#sourcelist-wavdetect
[3] https://cxc.cfa.harvard.edu/ciao/ahelp/chandra_repro.html
[4] https://cxc.cfa.harvard.edu/ciao/ahelp/fluximage.html
[5] https://cxc.cfa.harvard.edu/ciao/ahelp/wavdetect.html
[6] https://cxc.cfa.harvard.edu/ciao/ahelp/roi.html

source C, then target A would exclude source B, target B would exclude both A and C, and target C would exclude B. Targetbkg=target and bkgfactor=1 were also set parameters for *roi*. This processed each target's background separately and put a 1-pixel gap between the source and background regions. The *srcflux*[7] tool was then ran on each observation using the source coordinates found from *wavdetect*, the source and background regions from *splitroi*. The psfmethod parameter was set to arfcorr and an absorbed power law model was applied. The photon index was set to 1.5 and the absorption was set to be the galactic constant for each location.

Once the data was processed,we used other analysis tools to aid in the determination of the sources. Taking the files produced by *srcflux*, Jupyter notebook (a python language processor) was used to compile the counts and flux data for each source and calculate the hardness ratios (HR). The output was a csv file that is shown in Appendix B. The two hardness ratios refer to the Hard and Soft colors and can be calculated using the following equation:

$$(1) \quad HR = \frac{b-a}{b+a}$$

The errors in these calculations are determined via error propagated under Gaussian distribution:

$$(2) \quad \sigma_{HR} = \frac{2\sqrt{b^2\sigma_a^2 + a^2\sigma_b^2}}{(a+b)^2}$$

(Jin, Zhang and Wu 2006). In these equations, a and b can be the hard, medium, or soft counts in the X-ray bands. For the Hard Color, a is the medium counts and b is the hard.

[7] https://cxc.cfa.harvard.edu/ciao/ahelp/srcflux.html

For the Soft Color, a is the soft counts and b is the medium counts. The σ correspond to the error in those counts respectively.

DS9 was used to view the location of the detected sources and make note of which sources are within the Fermi source ellipses (also shown in Table 10 in Appendix B).

To understand how the X-rays are being generated by the sources we detected, spectral analysis is needed, that is applying spectral models to the plotted spectrum of a source. Before this can be performed, the spectrum must be extracted from the CXO data using *specextract*[8]. We customized this tool by settings the weight and correctpsf parameters to no and yes respectively. Weight=no tells the script to make a point-like ARF (auxiliary response file). While correctpsf=yes is set so that *arfcorr* will run the correct ARF. The spectrum file created by *specextract* is then loaded into XSPEC for plotting and fitting with models.

III.a.iii. Multi-Wavelength Methods

As previously discussed, it is difficult to classify an object using only one electromagnetic spectrum. Once the X-ray data had been processed, the next thing to do was compare the locations of the X-ray sources to those any known objects. Importing the Appendix B table into TOPCAT (Tool for OPerations on Catalogues And Tables) and cross referencing the locations (right ascension (RA) and declination (DEC)) of sources in catalogs from Two Micron All Sky Survey (2MASS), Global Astrometric Interferometer for Astrophysics (GAIA), Wide-field Infrared Survey Explorer (WISE), and Panoramic Survey Telescope and Rapid Response System (Pan-STARRS), data for sources within 1.5" of the X-ray source's location was appended as new columns to the

[8] https://cxc.cfa.harvard.edu/ciao/ahelp/specextract.html

csv file produced by the python code. Aladin Lite was also used to look for interesting features in images from various observatories in different wavelengths at each observation's location. If something interesting was in the image, it could provide another clue as to what the source is.

IV. DATA

After processing the observational data, we found 100 sources across all 13 observations. The breakdown of how many sources were found in each observation is shown in Table 1 below. Significant sources had broad counts > 10 or a source significance > 3. Source significance is equivalent to signal-to-noise ratio and illustrates confidence of the source being real expressed in $sigmas$ (standard deviation) above background. Seven of these sources had high enough counts to perform spectral analysis on and are noted as bright sources.

Table 1: Summary of sources found in each observation. The RA and DEC are in sexadecimal format.

ObsID	Date	Target	Right Ascension	Declination	Significant Sources	Bright Sources
20324	2018/05/11	3FGL J1306.4-6043	13 06 27.50	-60 43 54.10	9	0
20325	2018/02/18	3FGL J1906.6+0720	19 06 41.10	+07 20 02.00	6	0
20326	2018/07/07	3FGL J1104.9-6036	11 04 59.40	-60 36 32.80	4	0
23586	2021/07/10	4FGL J1736.1-3422	17 36 06.22	-34 22 37.92	12	1
23587	2021/07/24	4FGL J1639.3-5146	16 39 23.50	-51 46 08.76	9	2
23588	2021/01/28	4FGL J1203.9-6242	12 03 56.23	-62 42 34.20	11	0
23589	2021/06/20	4FGL J0854.8-4504	08 54 48.84	-45 04 19.92	7	0
23590	2020/12/14	4FGL J2035.0+3632	20 35 01.70	+36 32 13.56	4	0
23591	2020/10/25	4FGL J2041.1+4736	20 41 10.94	+47 36 10.44	5	1
23592	2020/11/29	4FGL J1317.5-6316	13 17 31.30	-63 16 42.96	1	0
23593	2021/03/28	4FGL J1329.9-6108	13 29 56.98	-61 08 26.16	16	2
23594	2020/10/10	4FGL J0744.0-2525	07 44 03.38	-25 25 55.20	6	0
23595	2021/02/02	4FGL J1358.3-6026	13 58 23.54	-60 26 39.84	10	1

Figure 14, Figure 15, and Figure 16 show all Chandra observations smoothed with a gaussian radius of 5 and a sigma of 2.5. The X-ray sources were labeled in red with a letter to reference which observation they were found in as well as numbered based on the RA in ascending order. Also shown are the source ellipses from 4FGL with their Fermi labels in blue and the 3FGL (if present) in green along. Each image has a coordinate grid (in degrees) with the RA being the horizontal axis and the DEC being the vertical.

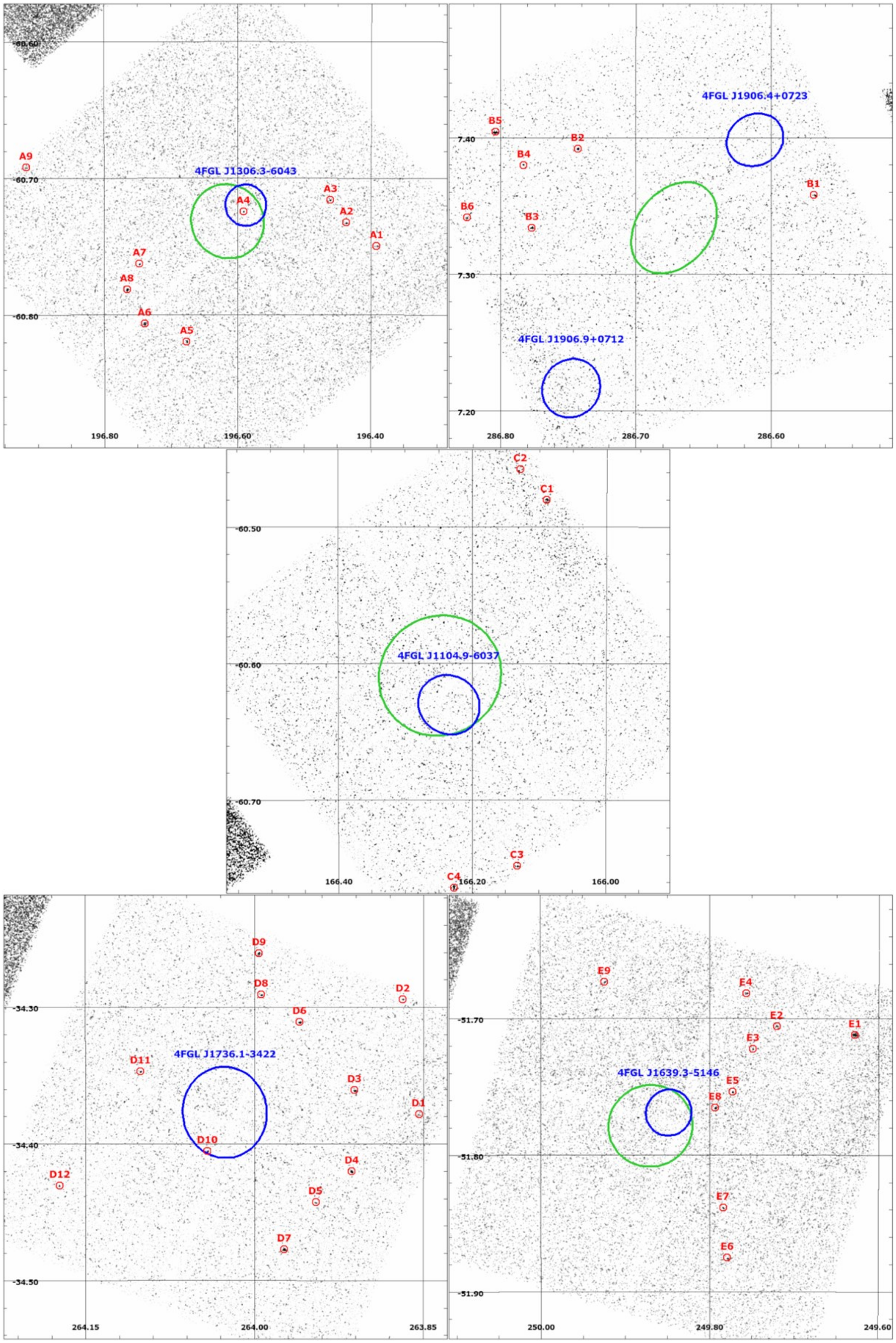

Figure 14: DS9 images of CXO observations 20324 (top left), 20325 (top right), 20326 (center), 23586 (bottom left) and 23587 (bottom right). Detected X-ray sources are circled and labeled in red, the 4FGL ellipses and labels in blue and the 3FGL ellipses (if present) in green.

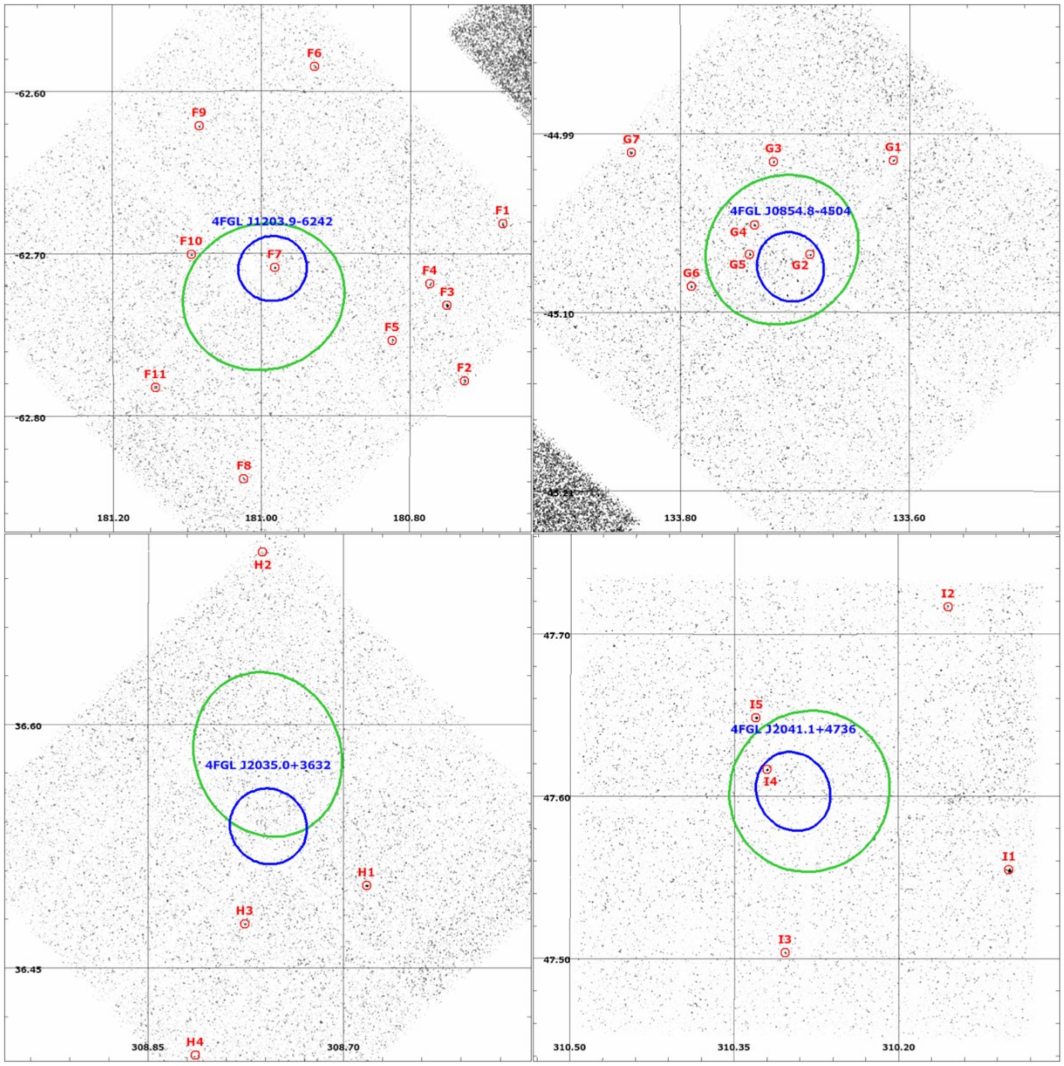

Figure 15: DS9 images of CXO observations 23588 (top left), 23589 (top right), 23590 (bottom left) and 23591 (bottom right). Detected X-ray sources are circled and labeled in red, the 4FGL ellipses and labels in blue and the 3FGL ellipses (if present) in green.

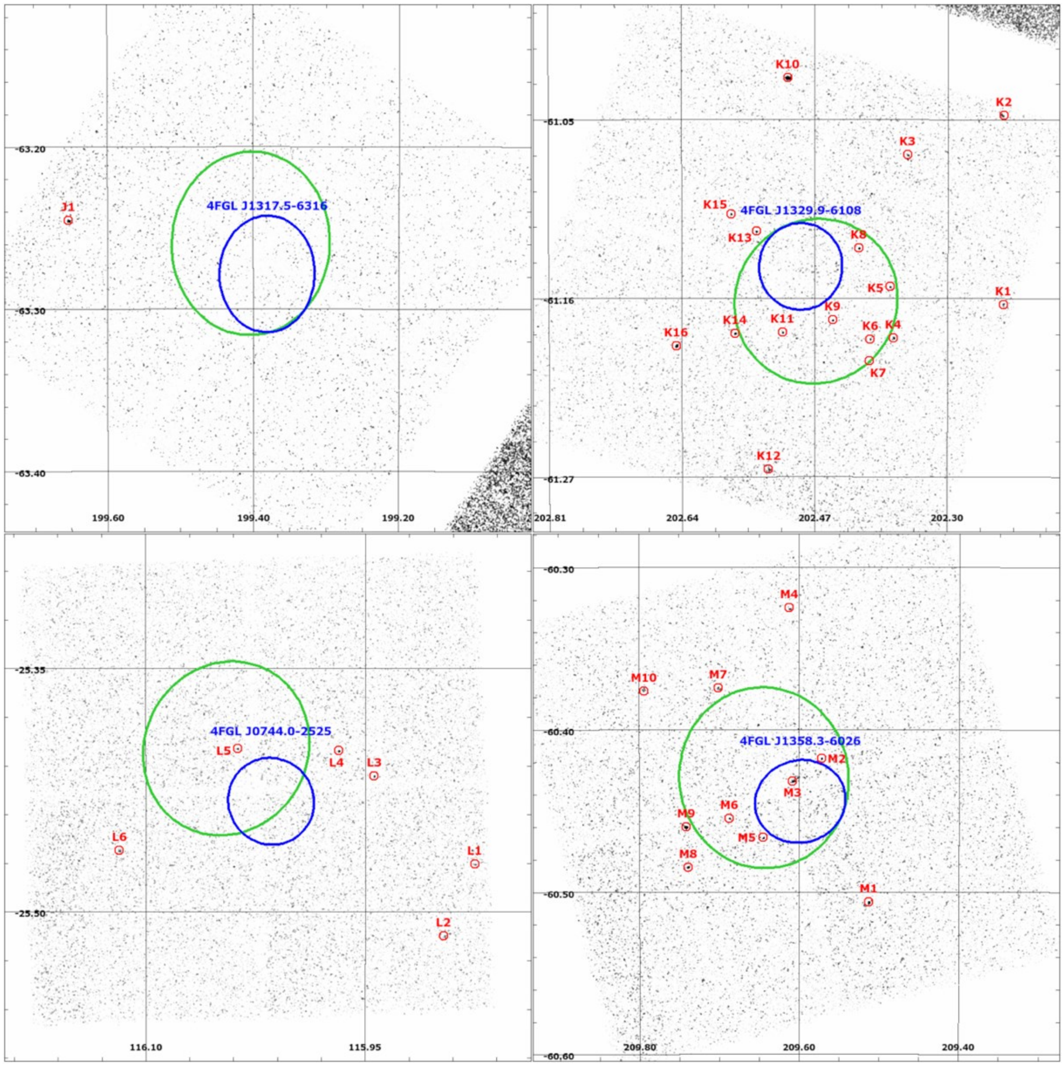

Figure 16: DS9 images of CXO observations 23592 (top left), 23593 (top right), 23594 (bottom left) and 23595 (bottom right). Detected X-ray sources are circled and labeled in red, the 4FGL ellipses and labels in blue and the 3FGL ellipses (if present) in green.

None of the sources within the Fermi ellipses had high counts, but there were seven sources outside of them that had counts high enough to attempt spectral analysis on. These bright sources, as well as the sources within a Fermi ellipse, are listed below in Table 2. These sources are all potentially interesting (based on either being bright sources or within the Fermi ellipses) and should be investigated further.

*Table 2: List of interesting sources found in the 13 CXO observations. The "Fermi Ellipse" column shows which Fermi ellipse the source was inside: 4 for the 4FGL, 3 for the 3FGL, 34 for both, and 0 for neither. The" MW Data" tells which observatory populated data from TOPCAT within 1.5" of the source's location: 2 for 2MASS, G for GAIA, W for WISE, P for PanSTARRS, and S for SDSS. Flux and Flux Error have units of $ergs\ cm^{-2}\ s^{-1}$. Sources with an * don't have flux data due to poor model fitting in srcflux.*

Source ID	Fermi Ellipse	MW Data	Source Significance	Broad Counts	Error Broad	Broad Flux	Error Flux Broad
K10	0		13.82	194.0	14	4.7E-13	5.6E-14
M9	0	2,G	10.34	109.8	11	2.3E-13	3.7E-14
E1*	0	W	9.00	91.2	10	-	-
K16	0	G	8.76	77.5	9	1.7E-13	3.2E-14
E8	0	2,G,W	8.66	75.7	9	1.5E-13	2.8E-14
I1*	0		7.02	56.2	8	-	-
D7*	0		7.05	53.1	8	-	-
I4	34		6.05	36.9	6	7.8E-14	2.1E-14
F7	34	G	5.21	27.7	5	4.9E-14	1.6E-14
K8	3	2,G,W	4.67	21.8	5	7.7E-13	2.7E-13
M5	3		4.51	20.9	5	3.4E-14	1.2E-14
K9	3		4.25	18.0	4	3.3E-14	1.3E-14
K7	3		4.12	16.9	4	3.7E-14	1.5E-14
D10	4	G,P	3.92	15.9	4	3.6E-14	1.5E-14
G5	3		3.80	15.0	4	2.4E-14	1.1E-14
G4	3		3.25	11.5	3	1.8E-14	9.3E-15
L5	3		3.25	11.0	3	5.5E-14	2.8E-14
M2	3		3.24	11.0	3	3.0E-14	1.5E-14
M6	3		3.25	11.0	3	2.6E-14	1.3E-14
K11	3	2,G	3.33	10.9	3	1.5E-14	7.6E-15
K5	3	G	3.22	10.8	3	2.6E-14	1.3E-14
M3	34	G	3.00	10.6	3	2.0E-14	1.1E-14
A4	34	2,G,W	3.10	10.0	3	1.2E-14	6.6E-15
G2	34		3.10	10.0	3	1.9E-14	1.0E-14
K6*	3		3.09	9.8	3	-	-

V. ANALYSIS

From all the observations, we found that some contained X-ray sources inside the 4FGL ellipse, some in the 3FGL ellipse, some in both and some in neither. This is noted in the "Fermi Ellipse" column with a 4, 3, 34, or 0 respectively in Table 2 (also Table 10 in Appendix B). The sources can also be seen in the DS9 images (Figure 14, Figure 15, and Figure 16).

V.a. XSPEC Modelling

As seen in Table 2 (also Table 8 in Appendix B), most of the sources have less than 50 counts across the broad X-ray spectrum. Spectral analysis on sources with such few counts will result in improper model fitting, if any at all. We took the top 7 sources (all of which had counts greater than 50) and performed spectral analysis on them. Unfortunately, none of these sources were within any Fermi ellipses. Another issue arises from the sources having such few counts; it made the model fitting difficult and thus determining the nature of the sources could be inaccurate. The spectra were limited to the energy range of $0.3 - 7.0\ keV$. All seven sources had an absorption model (*tbabs*[9]) applied to them to take care of the column density of the galaxy but had varying emission models applied: power law[10], blackbody[11], bremsstrahlung[12], apec[13], and mekal[14]. All sources had models applied to their spectrum without any binning of the counts, using the absorption abundance set to *wilm* (Wilms, Allen and McCray 2000), and using the CSTAT statistic. Using the *wilm* abundance allows the adjustment of the abundance for

[9] https://heasarc.gsfc.nasa.gov/xanadu/xspec/manual/node268.html
[10] https://heasarc.gsfc.nasa.gov/xanadu/xspec/manual/node216.html
[11] https://heasarc.gsfc.nasa.gov/xanadu/xspec/manual/node137.html
[12] https://heasarc.gsfc.nasa.gov/xanadu/xspec/manual/node144.html
[13] https://heasarc.gsfc.nasa.gov/xanadu/xspec/manual/node134.html
[14] https://heasarc.gsfc.nasa.gov/xanadu/xspec/manual/node193.html

each element individually. Even if the user doesn't set them manually, the model will adjust each element's abundance separately. *Tbabs* also "requires" the use of this abundance model. All sources had the absorbed power law applied to their spectra. The plots of this are shown in Figure 17 and the statistics in Table 3.

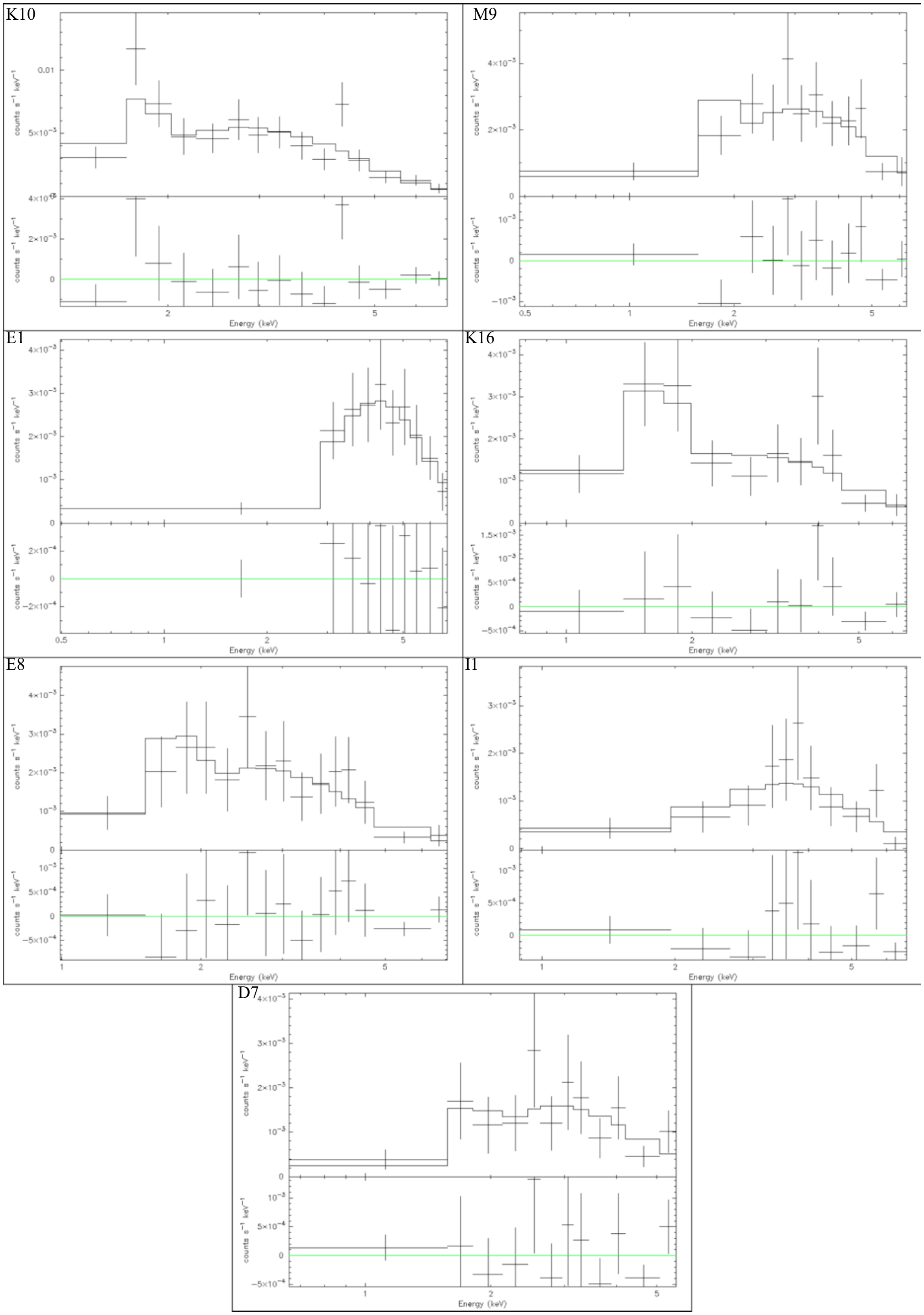

Figure 17: Plots of K10, M9, E1, K16, E8, I1, and D7 (left to right, top to bottom) spectrums fitted with the absorbed power law model. Below each plot is the fitting statistic error.

Table 3: Absorbed power law model fitting statistics for the bright sources. nH units: $\times\, 10^{22} cm^{-2}$

Source	Tbabs nH	nH error	Γ	Γ Error	Norm	Norm Error	Cstat	χ^2	D.o.f	Null Hyp
K10	2.7	0.9	1.9	0.4	2.7E-04	1.6E-04	122.8	146.0	136	0.3
M9	2.7	1.0	1.5	0.5	7.4E-05	5.1E-05	76.7	93.7	87	0.3
E1	11.2	6.2	0.9	1.0	5.4E-05	8.2E-05	66.6	70.1	79	0.8
K16	0.5	0.6	1.2	0.5	3.1E-05	1.9E-05	55.2	56.8	60	0.6
E8	3.2	1.1	2.3	0.6	1.3E-04	1.0E-04	53.9	51.5	69	0.9
I1	4.2	2.7	1.2	1.0	3.6E-05	4.2E-05	50.5	45.9	43	0.4
D7	4.7	2.2	2.4	0.9	1.8E-04	2.3E-04	29.6	25.0	44	1.0

If the distance was known, we could use the galactic absorption value (listed in Table 4) found using the location of the sources and the nH Column Density tool[15] on the HEASARC website ((HEASARC) 2014).

Table 4: Galactic column Density (absorption) for each source based on its RA and DEC.

Source	Galactic Absorption ($\times\, \mathbf{10^{22}}\ \boldsymbol{cm^{-2}}$)
K10	0.63
M9	1.21
E1	0.417
K16	0.705
E8	0.414
I1	0.828
D7	0.712

While applying the other models to the sources, some of them had better statistics than the absorbed power law model. In fact, the only sources where the absorbed power law was the best model was for K10 and K16. For the K16 source, the galactic absorption is within the error of the absorption factor. This means that the source is likely to be a galactic source. In contrast, the absorption factor is larger for K10 than the galactic

[15] https://heasarc.gsfc.nasa.gov/cgi-bin/Tools/w3nh/w3nh.pl

absorption. This could mean that there is other gas or dust particles between us and the source, indicating larger distance, or the presence of intrinsic (to the source) absorption.

For sources M9, E1, and I1, the absorbed blackbody model was best as shown in Figure 18 and Table 5. Absorbed mekal was best for source E8 (Figure 19 and Table 6) and absorbed apec was best for source D7 (Figure 20 and Table 7).

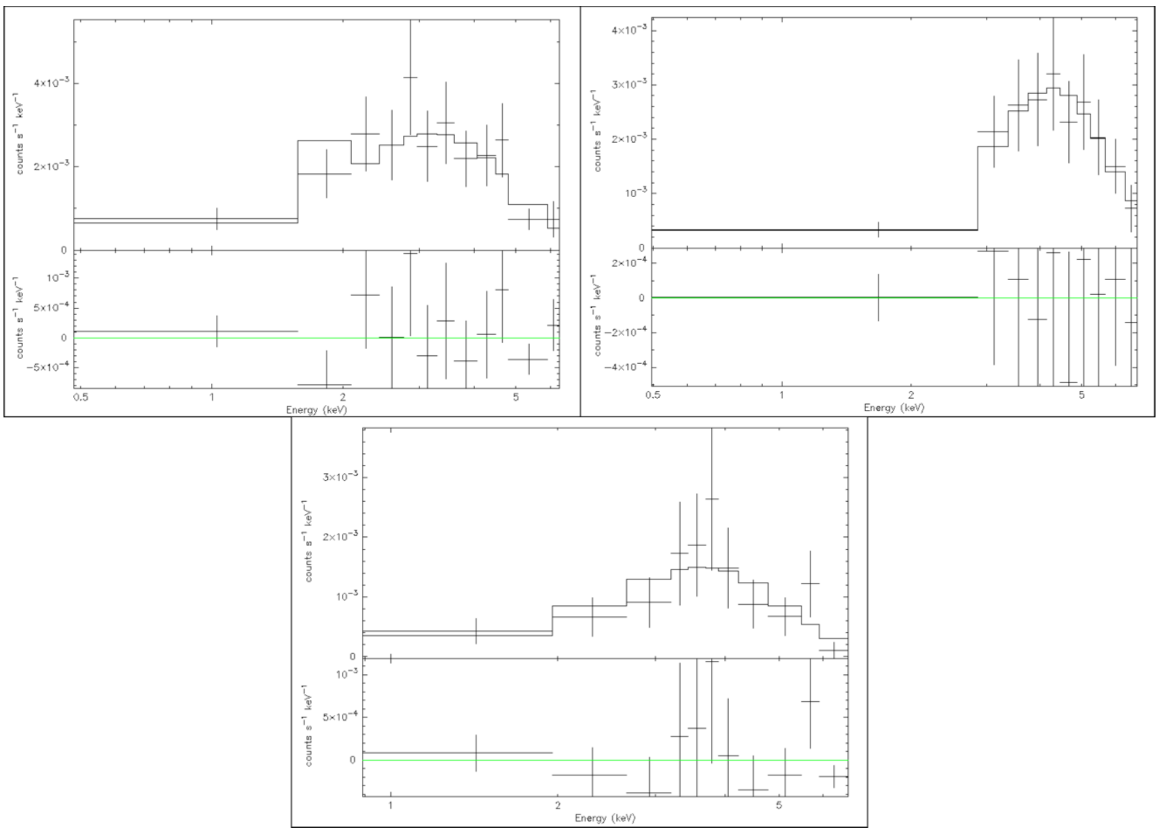

Figure 18: Spectrum plots with absorbed blackbody model fitted for sources M9(top left), E1 (top right), and I1(bottom center).

Table 5: Absorbed blackbody model fitting parameters and statistics. nH units: $\times 10^{22} cm^{-2}$

Source	Tbabs nH	nH Error	BB kT (keV)	kT Error	BB Norm	Norm Error	Cstat	χ^2	D.o.f	Null Hyp
M9	1.0	0.7	1.2	0.2	3.9E-06	5.5E-07	74.9	90.6	87	0.4
E1	8.5	4.6	1.9	0.8	1.1E-05	4.8E-06	66.3	69.8	79	0.8
I1	2.4	1.9	1.4	0.5	3.3E-06	9.5E-07	49.5	45.9	43	0.4

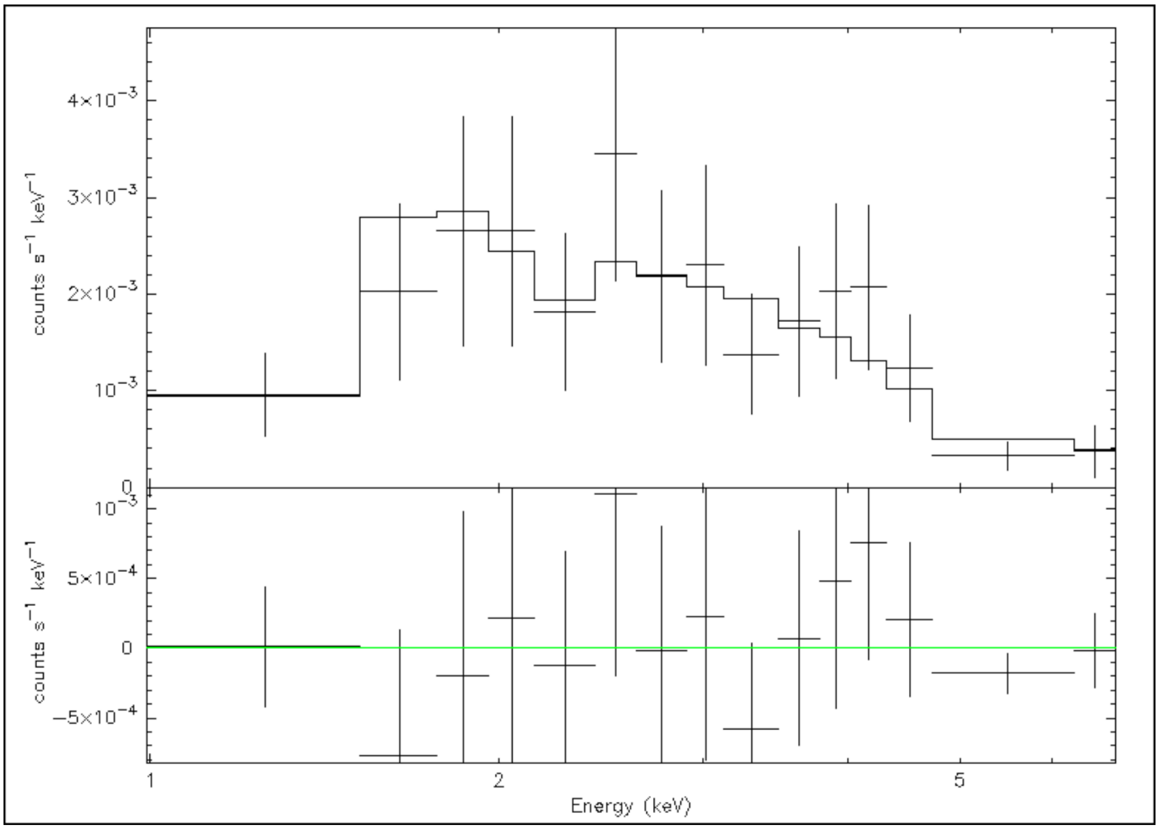

Figure 19: E8's spectrum plotted with the absorbed mekal model fitted. Bottom pane is the fitting statistic error.

Table 6: Absorbed mekal model fitting parameters and statistics for source E8. nH units: $\times 10^{22} cm^{-2}$

Source	Tbabs nH	nH Error	Mekal kT	kT Error	Mekal Norm	Norm Error	Cstat	χ^2	D.o.f	Null Hyp
E8	2.9	0.8	3.4	1.5	2.7E-04	1.0E-04	51.8	48.7	69	0.97

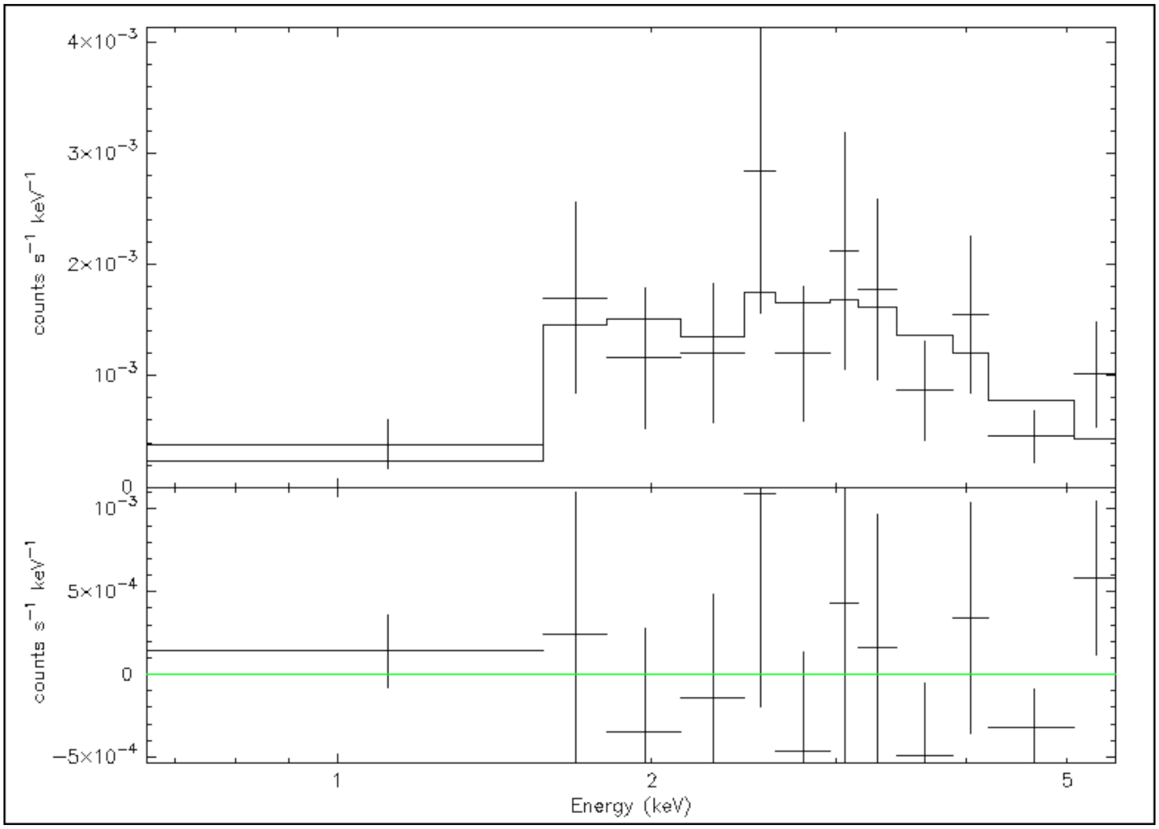

Figure 20: Source D7's spectrum plotted with the absorbed apec model fitted. Bottom pane is the fitting statistic.

Table 7: Absorbed apec model fitting parameters and statistics for source D7. nH units: $\times 10^{22} cm^{-2}$

Source	Tbabs nH	nH Error	Apec kT (keV)	kT Error	Apec Norm	Norm Error	Cstat	χ^2	D.o.f	Null Hyp
D7	4.5	1.5	3.0	1.5	3.8E-04	2.0E-04	29.4	24.6	44	0.99

I also tried to use a more complex model when fitting these spectra. That is to combine the absorbed power law with two other models listed above. However, the limited number of counts made such attempts infeasible.

V.b. Color-Color Diagram

As mentioned before, another useful way to analyze observation data is using hardness ratios in a color-color plot. Plugging the medium counts for a and the hard counts for b in equation 1 gives the hard color (equation 3). While plugging in the soft counts for a and the medium counts for b into equation 1 gives the soft color (equation 4). Their errors can be calculated by plugging in the same values into equation 2. Both colors and their errors are shown in Table 10 in Appendix B.

$$(3) \quad hard\ color = \frac{H - M}{H + M}$$

$$(4) \quad soft\ color = \frac{M - S}{M + S}$$

The results of plotting these ratios can be seen below Figure 21. Overlaid on the color-color plot is simulated counts for various accretion disk models: disk blackbody, power law with varying photon index Γ, and power law model with varying hydrogen column density (nH; the blue, purple, and red lines, respectively, in Figure 21). For the varying photon index power law model, Γ goes from 0.4 to 4. For the varying column density power law model, Γ is fixed at 2.0 and nH has the following values: 0, 0.1, 0.5, 1.0, 2.0, 5.0, and 10.0 ($\times\ 10^{22} cm^{-2}$). The temperatures of the disk blackbody model are 0.1, 0.2, 0.3, 0.4, 0.5, 0.8, 1.0, 2.0, 5.0 and 10.0 kT. Note that the average error of the hardness ratios (shown as the cross hair in the upper left corner of the plot) is large. This means that there are numeral sources that could shift to be on one of these models. Sources with zero counts in an energy band will result in one of the HR coordinates being 1 or -1 (depending which band has zero counts) and a shift to the edge of the plot. This can because by a source being very faint or highly absorbed (absorption affects primarily the soft, and, in part, the medium bands).

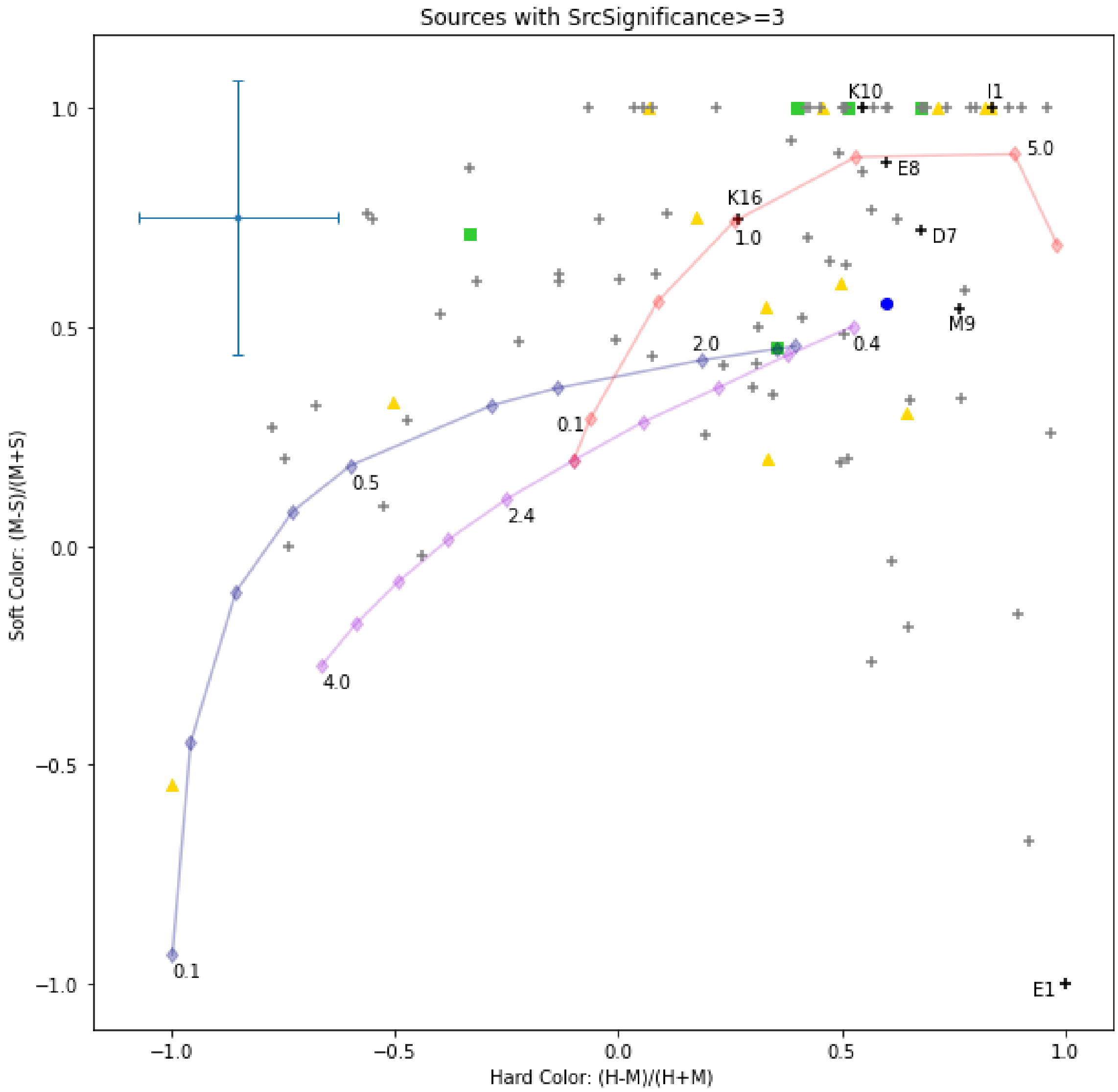

Figure 21: Color-color plot of the Hard vs Soft X-ray colors for all 100 sources detected. Sources within the 4FGL ellipse are represented by a blue circle. Sources in the 3FGL ellipse are marked with a yellow triangle. Sources in both Fermi ellipses are shown as green squares. Sources not in any Fermi ellipse are shown as grey crosses, except for the bright sources which are black and labeled. A disk blackbody is shown in blue and a power law in purple. The effects of absorption are shown in red for a power law with $\Gamma=2$.

Looking back to the top seven count sources, we can make note of where they are on this graph as another tool for characterizing these sources. Note that the hardness of these sources (seen in Appendix B) could also be skewing their locations toward the edge of the color-color plot. Sources K10 and I1 which have zero counts in the soft X-ray band are pushed to the top of the plot. Thus, the nearest model is absorbed power law model (the transparent red line with diamond points in Figure 21) at the points corresponding to $nH = 2.0 \times 10^{22} cm^{-2}$ and $nH = 5.0 \times 10^{22} cm^{-2}$, respectively. D7 (0.68,0.72) also has mostly hard X-ray counts and could be shifted towards the $nH = 5.0 \times 10^{22} cm^{-2}$ point. There are also two sources that lie on or extremely close to the absorbed power law model, K16 and E8. The K16 source, located at (0.27, 0.74), is right on the $nH = 1.0 \times 10^{22} cm^{-2}$ point, while the E8 source is at (0.59, 0.875) and near the $nH = 2.0 \times 10^{22} cm^{-2}$ point. M9 also appears to be highly a highly absorbed source. The source E1 is unique in the fact that all of its counts are in the hard X-ray band. This results in it being at the point (1,-1) and nowhere near any of the models.

We can also see from Figure 21 that there is a source (K8) within the 3FGL ellipse (as marked with a yellow triangle) and at the color-color plot point of (-1, -0.54). This lower left-hand corner of the color-color plot is synonymous with super soft sources. Although K8 lies in this region, the low total counts it has (~21.8) means that more information is needed to categorize this source. In fact, the majority of the X-ray sources, and all of the bright ones, are located in areas of the plot that are associated with moderate or high galactic column density. This makes classification of these sources extremely difficult if one relies only on the X-ray data.

V.c. Multi-Wavelength Analysis

All of the observations were inspected with Aladin Lite to see what other large-scale structures are present in other wavelengths. Nothing was found: no SNR nor molecular clouds are seen in the images.

We looked in the 2MASS, GAIA, WISE, and Pan-STARRS catalogues for data that correlated to sources that were within 1.5” of our detected X-ray sources’ locations. 2MASS and WISE observe in the infrared spectrum with 2MASS being a ground-based and WISE being space-based. Similarly, GAIA and Pan-STARRS observe in the optical with Pan-STARRS being ground-based and GAIA being space-based.

Of the top seven sources, M9, E1, K16, and E8 have data from other observatories. While it is possible that sources with populated data could hint towards these sources existing in binary systems, the counts of these objects are too low to definitively say what type of binary system these are.

VI. CONCLUSION & FUTURE WORK

Due to the low number of counts in most of the sources, as well as none of the top seven sources being within any Fermi ellipses, definitive classifications cannot be obtained. Speculation on what the top seven sources is done below. There are also other sources outside of the top seven that could exist in a binary system due to the proximity to other sources detected by other observatories. The optical counterpart's (as seen with GAIA or PanSTARRS) emission is not likely absorbed and thus the object could be close in our galaxy. The same goes for sources that had data detected in WISE due to its NIR observation capabilities. Sources that have data from 2MASS, GAIA, and WISE could be stars that are close enough for the X-rays from their stellar corona to be detected. For sources without counterparts found in other observatory's catalogs, they could be extremely faint, isolated pulsars.

We have identified six γ-ray sources for which we have a possible X-ray counterpart. Unfortunately, all X-ray counterparts do not have sufficient counts for a proper spectral analysis. However, four of them (A4, D10, F7 and M3) have lower energy counterpart(s), while the rest have no counterpart at other wavelengths (G2 and I4). Due to the unknown distance to these sources, it is difficult to determine the type of binaries (if that is the true nature) these are. For example, F7 and M3 are only detected with GAIA. This suggests that these sources were too faint for the other shallower surveys to detect, meaning, F7 and M3 are unlikely to be nearby sources. The same can be said about D10, which has GAIA and PanSTARRS data. All three have highly absorbed X-ray properties. A4, on the other hand, has counterparts in GAIA, 2MASS and WISE (no

PanSTARRS). However, its X-ray spectrum is also highly absorbed. This may suggest a not-too-distant source with intrinsic (to the system) X-ray absorption, such as an XRB.

G2 and I4 have no counterparts in the optical, NIR or IR. There are three possible explanations for this. An isolated pulsar will not be detectable in the lower energy wavelengths. The light from an AGN seen through the disk of the Milky Way will also be very absorbed, thus leaving only X-rays for us to detect. However, the Chandra observing program was designed to avoid AGNs (based on γ-ray selection criteria), making AGN an unlikely identification. The last possibility is an XRB on the other side of the galaxy.

Three other γ-ray sources have X-ray sources right outside the γ-ray uncertainty ellipses. These X-ray sources could be the true γ-ray counterparts.

Lastly, we have four γ-ray sources without any potential X-ray counterpart. It is possible that the true X-ray counterpart is too faint to be detected by our short observing program. It is worth noting that there exists a class of γ-ray sources called "dark accretors" due to their lack of lower energy (including X-rays) counterparts to the γ-ray emission. The nature of these sources remains a mystery.

One of the other outside of the top seven that should be talked about is the source K8. K8 lies in the super soft source region of the color-color plot and is within the 3FGL ellipse. K8 also has data in the 2MASS, GAIA, and WISE catalogs. As sated above, it could be a nearby star whose stellar corona is emitting X-rays. This would explain the soft nature of the X-ray emission. Unfortunately, the counts for this source were too low to run a spectral analysis on.

VI.a. **K10**

K10 was the highest count source detected from all 13 observations, with ~193 counts. Despite this, its spectrum didn't produce a great model fit for any of the models we tested. Two models came close: the absorbed power law and the absorbed apec. However, the apec model had high errors and there was no possible companion data generated from TOPCAT. The color-color plot also suggests that the best model is an absorbed power law. Although, with most of the counts being in the hard X-ray band and zero in the soft band, this could be skewed. The absorbed power law model along with no counterparts suggests the source could be an isolated pulsar.

VI.b. **M9**

M9 has data from 2MASS and GAIA sources within 0.5" of its location as well as the second highest counts detected (~109). M9's spectrum is best fit by an absorbed blackbody model with the galactic absorption falling within the model's nH parameter error. Having an optical counterpart and not highly absorbed suggests that the source is close by in our galaxy. The fact that the best fit model is a blackbody and M9 has optical and infrared data for a possible companion says this should be a nearby binary system.

VI.c. **E1**

E1 had data from WISE and ~93 counts detected in X-rays, ~91 of which are in the hard X-ray spectrum. This points towards the source being an AGN with the soft and medium X-rays being absorbed in our galaxy. Although, verifying this is difficult due to the low number of counts.

VI.d. **K16**

With only ~77 counts, finding a model to fit K16 was difficult. The best fit was the absorbed power law that had the galactic absorption within the column density error. The color-color plot seems to confirm a power law model with the absorption $nH = 1.0 \times 10^{22} cm^{-2}$. However, due to the faintness of the source, this is very uncertain. K16 also had optical data from GAIA which implies this could be a binary system. Regardless, the low number of counts makes determining if the column density is an intrinsic value to the source or due to its distance.

VI.e. **E8**

The cstat statistic for the spectra models tested on E8 vary only slightly and made determining the best fit difficult. The low number of counts attributes to this inconclusive model fitting and shifts the location to the top right of the color-color plot. Perhaps the most interesting aspect of this source is that data was found within 1.5" of this source in 2MASS, GAIA, and WISE. This with mostly hard X-rays and the column density being much greater than the galactic absorption value hints that E8 could be an AGN shining through our galaxy or a nearby star.

VI.f. **I1**

Source I1's hardness ratios suggests an absorbed power law model. Its low number of counts are dominant in the hard X-ray spectrum and are likely disrupting proper color-color plotting. With no counterparts at lower energies, the source could be an isolated pulsar. As with every other source we detected, classification is indeterminate due to the low number of counts detected and further observation is needed.

VI.g. **D7**

The least counts of the bright sources, D7 had even smaller margins for picking the best fit model. The absorbed apec model's cstat was only slightly better than the mekal and power law models. Bad model fitting along with no multi-wavelength data, makes classifying this source extremely difficult. The color-color plot suggests this source should have an absorbed power law model with $nH = 2.0 \times 10^{22} cm^{-2}$. Based on this, the source could be a pulsar.

VI.h. **Future Work**

While this work sheds some light into what these 13 γ-ray sources could (or could not) be, further investigation is needed to narrow down the possible nature of some of these sources. This will be done using three main approaches.

First, an automated machine learning (ML) classification tool will be utilized to process all available data in the archives and provide a classification (and confidence level) for each source. This tool uses a training dataset of literature verified sources to learn from. The ML pipeline is currently being finalized (develop by collaboration between Texas State University and George Washington University) and will be used, when completed, on the 13 γ-ray sources we discuss here.

Second, for the sources in the Fermi uncertainty radii, proposals for deeper follow up observations with the Chandra X-ray Observatory or the XMM-Newton telescope will be submitted. Thus, a larger number of counts can be detected that will allow proper spectral analysis to determine the physical processes behind the emission of these selected sources.

Lastly, for X-ray sources within the Fermi ellipses lacking any optical counterparts, we will propose follow up optical/NIR observations. We will target large telescopes (such as the Very Large Telescope in Chile or the Keck Observatory in Mauna Kea, Hawaii) that go far beyond the limitations of the shallow surveys used in this work. Completing the multi wavelength picture of these sources is crucial to understanding their nature.

APPENDIX SECTION

APPENDIX A: DETAIL ON ANALYSIS TOOLS

I. CIAO (Fruscione, et al. 2006)

Due to data from CXO being 4-dimensional (2 spatial, energy, and time) with each dimension having elements that can be individually analyzed, CIAO was built to handle data with any number of dimensions and analysis on said data without having to worry about which axis was being analyzed (and no built-in assumptions toward any of the spatial, time, energy nor any other variable. This allows CIAO to treat each axis as independent during analysis.). Despite being developed for the CXO, CIAO is mission independent and can be used for analyzing other X-ray and non-X-ray missions. Tools within CIAO are divided into seven main categories: data manipulation, data preparation (note: calibration files needed for standard processing and analysis are located withing the directory called Chandra Calibration Database (CALB)), imaging, imaging spectroscopy, grating spectroscopy, timing analysis, and response tools. Data processing threads are located on the CIAO website () for users to learn how to analyze CXO data. CIAO tools use a variety of parameters when running. Some of which are required, while others are optional and used to fine-tune the scripts processing of data. Any parameter that isn't set by the user, will run under the default values set by CIAO. Some common parameters for CIAO tools are mode and clobber. By setting mode=h, we can turn off the prompting of any unset parameters and instead use only the parameters in the command line or parameter file. Clobber (clob)is a parameter that tells CIAO if you want to overwrite existing output files. To overwrite, you would set clobber=yes (or clob+).

Tools that were used in my research are listed below. (Tools used in my data processing tree are detailed below.)

I.a. Chandra_repro

The *chandra_repro* tool initializes a reprocessing script based on the recommended data processing steps in the CIAO analysis threads. It reads from the primary and secondary data directories and creates a new bad pixel file, a new event file and a new Type II PHA file with the appropriate response files. The script then stores the newly created files in a directory called repro (this can be customized by changing the *outdir* parameter).

I.b. Fluximage

The *fluximage* script takes event files and any specified bands (energy levels) and creates exposure-corrected images of the observation. It also automates the creation of aspect histogram, instrument, and exposure maps. Some of the parameters that can be customized to fit the user's needs are the bands, binsize, and psfecf. The bands parameter selects which energy levels (in keV) are used in the creation of the images and maps. One can use the short-hand notation "csc" when setting the band parameter to denote that you want the soft, medium, and hard bands. Bin size refers to the image binning factor which groups adjacent pixels together into a larger single pixel. For refence, binsize=4 generates images with pixels that are 1.986 arcseconds (for an ACIS observation) or 0.5272 arcseconds (for HRC observations) in size. The psfecf parameter tells *fluximage* to create a PSF (point spread function) map image that has the ECF (encircled counts fraction) specified (in arcseconds) for each pixel.

I.c. <u>Wavdetect</u>

The *wavdetect* tool is a combination of two other tools: *wtransform* and *wrecon*. It first runs *wtransform* which analyzes an image file and detects possible source pixels by comparing it with “Mexican hat” wavelet functions of different sized scales. Then it runs *wrecon* to generate the source list based on information from each wavlet scale by comparing sources detected in each scale. A cell is computed that contains most of the source’s flux and all the source properties are assigned to that cell. As stated above, the parameter that we modify for our analysis is the scales parameter. The scales parameter sets the wavlet radii (in pixels) and has values of 2^n. In our analysis processing tree, we also specify the regfile, expfile, and the psffile. The regfile parameter sets the file for ASCII region output. The expfile parameter sets the input exposure file. The psffile parameter holds the observation specific PSF size data (generated by the same image used during the fluximage or mkpsfmap tools).

I.d. <u>Roi and splitroi</u>

The *roi* tool uses the position and shape of sources from a source list and creates source and background regions for each non-overlapping source region. If sources are close enough together that their regions overlap, *roi* may consider these as a single source. For sources located in the background region of another source, the source is subtracted from said background.

Splitroi then takes all the output files from *roi* and merges all the source regions into a single file and all the background regions into a single file. This is helpful when you want to load all the source regions in an observation image.

I.e. Srcflux

Srcflux is a tool that calculates the count rates and flux for sources in given source and background region files (if supplied). It uses another tool called *aprates* to calculate the count rates and uses Bayesian statistics to determine the certainty of the calculations (called credible interval). Srcflux can estimate the flux in three different ways: 1. A model independent way using the tool called eff2evt; 2. A model-dependent estimate using the tool *modelflux*; 3. Calculating flux in photon units using the *fluximage* tool to create exposure and correction images. The results of srcflux are written to one or multiple output files (one for each energy band) that have one source per row. The easiest way to use this tool is to specify the positions of the sources but not use source or background region files. The tool then creates a circular region around each position that encompasses 90% of the PSF at 1.0 keV. If source and background files are specified, the position parameter is still needed for the PSF fraction correction. This can be found in five different ways that is controlled through the psfmethod parameter. The parameters we set to process the data were bands, srcreg, bkgreg, psfmethod, model, paramvals, absmodel and absparams. Just like with *fluximage*, bands sets the energy levels you want included in the analysis. Srcreg and bkgreg set the source and background region files respectively. The psfmethod parameter sets the method for how to compute the PSF fraction in the source and background regions. There are five different methods it can achieve this: ideal (assumes the source region contains 100% of the source flux while the background region contains 0%), quick (uses the radius of the source regions to look up the PSF fraction for the specified energy bands while the background region is set to 0% source flux), arfcorr (runs the arfcorr tool on the source and background regions at each specified energy band and calculates the PSF fraction via a model PSF), psffile (uses an image of the PSF by setting the psffile parameter), and marx (lets the user run MARX to simulate the PSF at the source locations at the characteristic energies for each energy band specified).The model parameter sets the Sherpa model expression for calculating the flux and count rate via the tool *modelflux*. Paramvals set the model parameters for the Sherpa model. The Absmodel parameter specifies the absorption model component of the Sherpa model with the absorption parameters being set in the absparams parameter.

I.f. Specextract

Specextract is a tool that creates source and background (optional) spectra for Chandra imaging-mode. In order to run this tool successfully, the user needs to make a few decisions: is the source's spatial extent large enough that the ARF and RMF should be weighted by the count distributions within the aperture; if weight=no, should the ARF be corrected to account for X-rays that are outside of the aperture; does the user want a background spectrum created as well and linked to the source spectrum; lastly, if there are multiple regions, shall the counts be added together into a single spectrum or should there be a separate spectrum for each region. These decisions can be made by customizing the parameters within *specextract*. The infile parameter for this tool is an event file with a filter that defines the region for the spectrum. The outroot parameter is the location of the output files (ungrouped and grouped source spectra, ungrouped and grouped background spectra, and weighted source and background RMF and ARF files). This tool makes use of other tools to perform its intended function. These tools are *dmextract*, *mkwarf* OR *mkarf*, *mkrmf* OR *mkacisrmf*, *dmgroup*, *dmhedit*, *dmmakereg*, *sky2tdet*, and *arfcorr*.

II. <u>TOPCAT (Taylor 2005)</u>

TOPCAT is an interactive graphical viewer and editor for tabular data. It was designed (and is kept updated) to provide astronomers most of the tools needed to perform analysis and manipulation of source catalogs and other data tables. Since some source catalogs can be millions of rows and columns, the main function is to easily explore these large data sets. TOPCAT provides numerous ways to view and analyze data such as a browser for the cell data, viewers for information about the table and columns, sophisticated single- and multi-dimensional visualization, calculating statistics and also appending multiple data tables using matching algorithms. TOPCAT provides a variety of output file formats and also works with non-astronomical data.

III. <u>Aladin lite (Boch and Fernique 2014)</u>

Aladin lite is a lightweight online version of Aladin Sky Atlas (Aladin) that runs in a browser. Both Aladin and Aladin lite provide an interactive visualization tool used for viewing astronomical images. By providing a target location (RA, DEC), the user can view survey images from a variety of observatories across the electromagnetic spectrum. Observatories available in Aladin lite are GLIMPSE360, Fermi, XMM/PN, Chandra, GALEXGR6/AIS, DSS2 (in red, blue, or composite), Mellinger, Finkbeiner, SDSS (data release 9), VTSS/Ha, PanSTARRS (data release 1 in color), DECaPS (data release 1), DECaLS (data release 3), 2MASS, SPITZER, allWISE, IRIS, and AKARI/FIS. It allows the user to overlay the images with source catalogues from GAIA (early data release 3) and 2MASS, as well as from SIMBAD (a dynamic astronomical database). Aladin lite allows for zooming in and out to the field of view limits of 180º and 0.01”.

IV. SAOImageDS9 (Joye and Mandel 2003)

Also known as just DS9, SAOImageDS9 is an astronomical imaging and data visualization application. DS9 has a multitude of features including 2-D, 3-D, and RGB frame buffers, mosaic imaging, tiling to see multiple images at once, blinking through image frames, geometric marking of regions, colormap manipulation, custom scaling via algorithms, arbitrary zoom, cropping, rotation, pan, and several coordinate systems. While using DS9, the user can also increase the binning parameter for FITS event files, import source catalogues, apply smoothing or contour paramters, and overlay the image with a coordinate grid.

V. XSPEC (Nasa High Energy Astrophysics Science Archive Research Center (HEASARC) 2014)

XSPEC is an X-ray spectrum fitting program designed to be detector independent so that it can be used for any spectrometer. It can be downloaded as part of NASA's High Energy Astrophysics Science Archive Research Center HEASoft software package. This package includes a variety of other software programs that are beneficial when preforming analysis on X-ray data. The software programs included are XANDU (which includes XSPEC), FTOOLS (used for manipulating FITS files), FITSIO (used for reading and writing FITS files), fv (used to view and edit FITS images and tables), and XSTAR (used to calculate the physical conditions and emission spectra.

APPENDIX B: LIST OF ALL SOURCES

Table 8: List of all 100 sources with their location (RA, DEC), source significance, counts and count errors. Note: RA and DEC are in degrees.

Source ID	RA	DEC	Source Significance	Broad Counts	Broad Error	Soft Counts	Soft Error	Medium Counts	Medium Error	Hard Counts	Hard Error
A1	196.3911787	-60.74974281	3.27	13.0	4	0.4	1	2.7	2	9.9	3
A2	196.4364022	-60.73260252	3.81	15.5	4	0.0	0	1.0	1	14.7	4
A3	196.4605246	-60.71603891	4.12	18.2	4	1.7	1	12.9	4	3.6	2
A4	196.5905766	-60.72451597	3.10	10.0	3	1.0	1	6.0	2	3.0	2
A5	196.6757496	-60.81963334	3.99	17.7	4	0.0	0	2.7	2	15.0	4
A6	196.7388114	-60.80654819	5.58	33.0	6	0.0	0	12.9	4	20.1	5
A7	196.7464873	-60.76277631	3.58	12.9	4	5.0	2	6.0	2	1.9	1
A8	196.7652172	-60.78159804	5.49	30.7	6	0.0	0	9.0	3	21.9	5
A9	196.9158007	-60.69188525	3.00	11.9	4	1.5	1	3.6	2	6.8	3
B1	286.5680796	7.3578098	2.17	13.3	6	3.6	3	2.1	3	7.5	5
B2	286.7423414	7.391812874	4.70	22.6	5	4.0	2	13.0	4	5.6	2
B3	286.7763234	7.33371363	4.42	23.0	5	0.0	0	2.4	2	21.1	5
B4	286.782392	7.379705929	3.19	13.1	4	0.7	1	5.5	2	6.9	3
B5	286.8033003	7.403903991	6.01	42.3	7	0.5	1	12.9	4	29.0	6
B6	286.8241141	7.341417848	2.80	13.3	5	1.9	2	4.0	2	7.4	4
C1	166.088414	-60.48035496	4.65	27.3	6	0.5	1	6.1	3	20.7	5
C2	166.1281685	-60.45814358	3.55	20.0	6	1.6	2	4.6	3	13.8	5
C3	166.1318958	-60.74834703	3.44	14.1	4	1.7	1	7.0	3	5.3	3
C4	166.2266571	-60.76431008	5.23	35.4	7	0.4	1	0.6	1	34.5	6
D1	263.8535382	-34.37848975	3.06	17.0	6	0.5	1	1.9	2	14.7	5
D2	263.8681622	-34.29440075	2.28	10.0	4	1.7	1	1.6	2	6.7	4
D3	263.9107671	-34.36100031	5.06	27.6	5	1.9	1	1.4	1	24.4	5

Source ID	RA	DEC	Source Significance	Broad Counts	Broad Error	Soft Counts	Soft Error	Medium Counts	Medium Error	Hard Counts	Hard Error
D4	263.9133198	-34.42045261	5.98	36.5	6	1.7	1	10.0	3	24.7	5
D5	263.9450595	-34.44300287	3.26	12.5	4	1.7	1	2.6	2	8.1	3
D6	263.9594204	-34.31121566	5.19	26.7	5	0.0	0	2.9	2	23.9	5
D7	263.9732532	-34.47752773	7.05	53.1	8	1.4	1	8.4	3	43.3	7
D8	263.9936167	-34.29111472	3.73	15.1	4	0.0	0	3.7	2	11.5	3
D9	263.9956556	-34.26061407	4.62	26.7	6	1.4	1	6.2	3	19.1	5
D10	264.0412224	-34.40556382	3.92	15.9	4	0.9	1	3.0	2	12.0	3
D11	264.1007409	-34.34731363	3.80	15.0	4	0.0	0	2.0	1	13.0	4
D12	264.1723857	-34.4306483	3.08	13.1	4	5.6	2	5.4	2	2.1	2
E1	249.6278835	-51.71222662	9.00	91.2	10	1.9	2	0.0	1	91.1	10
E2	249.7200834	-51.70581353	3.02	10.7	3	-0.1	0	1.7	1	9.1	3
E3	249.7485102	-51.72236483	3.08	10.5	3	4.9	2	4.9	2	0.7	1
E4	249.7564706	-51.68201763	3.39	15.9	5	0.0	0	4.1	2	12.3	4
E5	249.7724178	-51.75395901	4.88	24.6	5	0.0	0	11.9	3	12.7	4
E6	249.7783692	-51.87525005	3.46	21.4	6	3.0	2	12.1	4	6.3	4
E7	249.7834429	-51.83863172	3.66	14.0	4	0.0	0	3.0	2	11.0	3
E8	249.7928277	-51.76565908	8.66	75.7	9	1.0	1	15.0	4	59.7	8
E9	249.9240045	-51.67361261	3.11	10.8	3	-0.4	0	6.0	2	5.2	2
F1	180.674683	-62.6815003	3.47	16.3	5	0.0	0	0.4	1	16.8	5
F2	180.7257215	-62.77838982	4.59	20.8	5	2.8	2	6.8	3	11.1	3
F3	180.749399	-62.73211319	6.01	40.0	7	7.7	3	13.0	4	19.2	5
F4	180.772517	-62.71887244	2.98	10.1	3	1.0	1	0.0	0	9.4	3
F5	180.8230046	-62.75361021	3.14	9.9	3	1.0	1	6.9	3	2.0	1
F6	180.9282876	-62.58485881	2.64	10.6	4	-0.8	0	3.1	2	8.2	3
F7	180.981562	-62.70878946	5.21	27.7	5	3.0	2	8.0	3	16.7	4

Source ID	RA	DEC	Source Significance	Broad Counts	Broad Error	Soft Counts	Soft Error	Medium Counts	Medium Error	Hard Counts	Hard Error
F8	181.0232625	-62.8392739	2.84	11.0	4	1.9	1	0.4	1	8.7	3
F9	181.0826557	-62.62170615	3.47	13.2	4	4.0	2	7.7	3	1.5	1
F10	181.0934222	-62.70084513	3.55	12.9	4	0.0	0	6.0	2	7.0	3
F11	181.1419458	-62.78264855	4.07	19.5	5	3.0	2	7.6	3	8.8	3
G1	133.6135096	-45.00647832	3.16	9.7	3	1.0	1	3.0	2	5.7	2
G2	133.6862155	-45.06463357	3.10	10.0	3	0.0	0	3.0	2	7.0	3
G3	133.718194	-45.00740617	3.34	11.6	3	0.0	0	1.9	1	9.7	3
G4	133.7348426	-45.04646553	3.25	11.5	3	1.0	1	1.9	1	8.6	3
G5	133.7390838	-45.06447677	3.80	15.0	4	0.0	0	7.0	3	8.0	3
G6	133.7901241	-45.08418616	3.05	10.8	3	0.9	1	1.7	1	8.2	3
G7	133.8421784	-45.00178704	3.99	18.1	4	1.7	1	7.5	3	8.9	3
H1	308.681807	36.50070611	5.88	35.5	6	1.9	1	8.9	3	24.7	5
H2	308.7613699	36.70597292	2.33	13.2	6	0.0	2	0.0	2	13.9	5
H3	308.7750245	36.47704194	3.13	10.6	3	0.0	0	5.0	2	5.6	2
H4	308.8132302	36.3959709	3.58	24.9	7	2.1	2	6.7	3	16.1	6
I1	310.0983526	47.55417908	7.02	56.2	8	0.0	1	4.6	2	52.0	8
I2	310.153454	47.71644133	2.57	12.6	5	0.0	1	3.2	2	9.8	4
I3	310.3029197	47.50353896	3.36	12.4	4	0.9	1	6.0	2	5.5	2
I4	310.3194362	47.61631769	6.05	36.9	6	0.0	0	6.0	2	30.9	6
I5	310.3294598	47.64836191	6.06	37.6	6	1.0	1	6.9	3	29.7	5
J1	199.6521931	-63.24564521	5.61	33.3	6	3.6	2	14.8	4	14.9	4
K1	202.2281006	-61.16392593	3.58	14.5	4	0.0	0	0.7	1	14.0	4
K2	202.2283639	-61.04754463	4.18	21.2	5	0.3	1	5.3	2	15.6	4
K3	202.3507796	-61.07166485	3.38	12.8	4	1.9	1	2.7	2	8.2	3
K4	202.3686145	-61.1845911	4.24	18.7	4	2.9	2	8.0	3	7.8	3

Source ID	RA	DEC	Source Significance	Broad Counts	Broad Error	Soft Counts	Soft Error	Medium Counts	Medium Error	Hard Counts	Hard Error
K5	202.3731583	-61.15297734	3.22	10.8	3	0.0	0	0.9	1	9.9	3
K6	202.3984784	-61.18530817	3.09	9.8	3	0.9	1	3.0	2	6.0	2
K7	202.3995382	-61.198884	4.12	16.9	4	1.0	1	4.0	2	11.9	3
K8	202.412969	-61.12929511	4.67	21.8	5	16.9	4	5.0	2	0.0	0
K9	202.4464135	-61.17359082	4.25	18.0	4	1.0	1	7.0	3	10.0	3
K10	202.503754	-61.02432728	13.82	194.0	14	0.0	0	44.0	7	150.3	12
K11	202.5106611	-61.18107761	3.33	10.9	3	3.0	2	6.0	2	2.0	1
K12	202.5284381	-61.26570073	4.67	23.5	5	2.8	2	11.8	3	9.0	3
K13	202.5440303	-61.11891871	4.59	20.8	5	6.0	2	10.9	3	3.9	2
K14	202.5713607	-61.18176832	5.05	24.9	5	0.0	0	5.0	2	19.9	4
K15	202.5762735	-61.10822914	3.29	10.9	3	4.0	2	6.0	2	0.9	1
K16	202.6463694	-61.1894152	8.76	77.5	9	3.9	2	27.0	5	46.7	7
L1	115.874818	-25.47062062	2.98	10.6	3	0.5	1	6.7	3	3.4	2
L2	115.8960122	-25.51489473	3.34	17.2	5	2.4	2	4.9	2	10.0	4
L3	115.9437117	-25.41655894	3.66	14.0	4	0.0	0	4.0	2	10.0	3
L4	115.9677948	-25.40095195	4.63	22.0	5	4.0	2	11.0	3	7.0	3
L5	116.0368413	-25.39947303	3.25	11.0	3	2.0	1	3.0	2	6.0	2
L6	116.1176165	-25.46238165	3.91	17.8	5	3.6	2	2.5	2	11.7	4
M1	209.5120853	-60.506347	4.29	20.0	5	6.7	3	11.7	3	1.5	1
M2	209.5715077	-60.41793876	3.24	11.0	3	0.0	0	3.0	2	8.0	3
M3	209.6079997	-60.43199592	3.00	10.6	3	0.0	0	2.6	2	8.1	3
M4	209.6118161	-60.32494079	2.80	13.6	5	0.7	1	1.5	2	11.3	4
M5	209.6442251	-60.46670035	4.51	20.9	5	0.0	0	3.0	2	17.9	4
M6	209.6865425	-60.45482897	3.25	11.0	3	0.0	0	1.0	1	10.0	3
M7	209.7003768	-60.37460722	2.78	10.3	4	0.0	0	0.0	0	11.3	4

Source ID	RA	DEC	Source Significance	Broad Counts	Broad Error	Soft Counts	Soft Error	Medium Counts	Medium Error	Hard Counts	Hard Error
M8	209.7385477	-60.48484497	5.53	30.9	6	0.0	0	7.0	3	23.9	5
M9	209.740898	-60.46013184	10.34	109.8	11	3.7	2	12.6	4	93.5	10
M10	209.7934138	-60.37637805	2.86	13.6	5	0.0	1	2.7	2	11.0	4

*Table 9: List of all 100 sources and their flux with errors. Flux units are $ergs\ cm^{-2}\ s^{-1}$. Note: some sources don't have flux data due to poor model fitting in srcflux and are marked with an *.*

Source ID	Broad Flux	Broad Error	Soft Flux	Soft Error	Medium Flux	Medium Error	Hard Flux	Hard Error
A1	4.5E-13	2.3E-13	4.0E-13	2.1E-12	2.1E-15	2.5E-15	3.7E-14	2.1E-14
A2*	2.7E-14	1.2E-14	-	-	6.7E-16	1.4E-15	3.0E-14	1.3E-14
A3*	3.0E-14	1.2E-14	-	-	1.0E-14	4.9E-15	2.1E-14	2.1E-14
A4	1.2E-14	6.6E-15	1.6E-15	3.4E-15	4.3E-15	3.1E-15	6.5E-15	6.9E-15
A5*	3.0E-14	1.2E-14	0.0E+00	-	2.2E-15	2.5E-15	2.8E-14	1.3E-14
A6*	6.3E-14	1.9E-14	0.0E+00	-	1.1E-14	5.0E-15	5.4E-14	2.1E-14
A7	2.6E-14	1.2E-14	1.6E-14	1.2E-14	6.6E-15	4.7E-15	3.1E-15	4.2E-15
A8*	4.7E-14	1.4E-14	-	-	6.3E-15	3.6E-15	4.3E-14	1.5E-14
A9*	1.3E-14	7.1E-15	-	-	4.1E-15	4.0E-15	2.3E-14	1.8E-14
B1*	-	-	-	-	1.5E-15	2.5E-15	4.6E-14	4.6E-14
B2	2.8E-14	9.7E-15	7.0E-15	6.3E-15	1.0E-14	4.8E-15	1.0E-14	7.7E-15
B3*	6.4E-14	2.4E-14	-	-	2.0E-15	2.7E-15	6.5E-14	2.5E-14
B4	1.4E-14	7.1E-15	5.5E-16	1.5E-15	4.1E-15	3.2E-15	9.2E-15	6.9E-15
B5*	8.4E-15	2.3E-15	-	-	1.1E-14	5.5E-15	5.7E-14	1.9E-14
B6*	-	-	-	-	4.0E-15	4.0E-15	2.5E-14	2.1E-14
C1*	-	-	-	-	7.0E-15	5.3E-15	5.3E-14	2.2E-14
C2	5.8E-13	2.7E-13	5.4E-13	9.3E-13	4.5E-15	4.5E-15	3.3E-14	1.8E-14
C3	3.2E-14	1.5E-14	8.0E-15	1.2E-14	8.0E-15	5.2E-15	1.6E-14	1.4E-14
C4*	9.6E-14	3.0E-14	-	-	1.1E-15	3.9E-15	1.1E-13	3.4E-14
D1*	-	-	-	-	2.0E-15	3.4E-15	7.3E-14	4.0E-14
D2*	-	-	-	-	1.3E-15	2.4E-15	2.1E-14	1.9E-14
D3	1.7E-13	5.7E-14	1.1E-13	1.5E-13	9.9E-16	1.8E-15	6.7E-14	2.3E-14
D4	1.1E-13	2.9E-14	3.5E-15	5.2E-15	1.2E-14	6.5E-15	9.3E-14	3.1E-14

Source ID	Broad Flux	Broad Error	Soft Flux	Soft Error	Medium Flux	Medium Error	Hard Flux	Hard Error
D5*	2.1E-14	1.1E-14	-	-	2.3E-15	2.8E-15	2.2E-14	1.4E-14
D6	5.8E-14	1.8E-14	0.0E+00	-	2.9E-15	3.1E-15	5.7E-14	1.9E-14
D7*	-	-	-	-	7.5E-15	4.6E-15	9.0E-14	2.3E-14
D8*	4.6E-14	2.0E-14	-	-	4.7E-15	4.4E-15	4.4E-14	2.2E-14
D9*	8.1E-15	2.9E-15	-	-	7.1E-15	5.2E-15	4.6E-14	2.0E-14
D10*	3.6E-14	1.5E-14	-	-	2.6E-15	2.7E-15	3.7E-14	1.8E-14
D11	5.0E-14	2.2E-14	0.0E+00	-	2.5E-15	3.4E-15	4.9E-14	2.3E-14
D12*	-	-	-	-	5.3E-15	4.2E-15	4.2E-15	6.7E-15
E1*	-	-	-	-	-	-	2.8E-13	5.0E-14
E2*	2.8E-14	1.6E-14	-	-	1.9E-15	2.9E-15	2.8E-14	1.7E-14
E3	6.1E-14	3.3E-14	5.3E-14	4.2E-14	4.9E-15	4.0E-15	1.1E-15	3.2E-15
E4*	6.5E-16	3.2E-16	-	-	4.4E-15	4.2E-15	1.6E-14	8.8E-15
E5	4.4E-14	1.5E-14	0.0E+00	-	1.0E-14	5.1E-15	3.4E-14	1.6E-14
E6*	-	-	-	-	1.2E-14	6.1E-15	2.8E-14	2.9E-14
E7	3.0E-14	1.4E-14	0.0E+00	-	3.1E-15	3.3E-15	2.8E-14	1.4E-14
E8	1.5E-13	2.8E-14	2.5E-15	5.3E-15	1.4E-14	6.2E-15	1.4E-13	2.9E-14
E9*	1.0E-14	5.4E-15	-	-	9.5E-15	6.8E-15	1.2E-14	9.8E-15
F1*	-	-	-	-	6.4E-16	3.4E-15	4.6E-14	2.1E-14
F2	6.2E-14	2.2E-14	1.1E-14	1.2E-14	1.1E-14	7.0E-15	4.0E-14	2.0E-14
F3	5.8E-14	1.6E-14	1.1E-14	7.1E-15	1.3E-14	6.5E-15	3.4E-14	1.4E-14
F4*	3.0E-14	1.7E-14	1.1E-14	2.3E-14	-	-	2.0E-14	1.2E-14
F5	2.6E-14	1.4E-14	2.8E-15	6.3E-15	9.9E-15	6.3E-15	1.3E-14	1.8E-14
F6*	-	-	-	-	3.2E-15	3.7E-15	2.7E-14	1.9E-14
F7	4.9E-14	1.6E-14	6.1E-15	6.5E-15	7.6E-15	4.6E-15	3.6E-14	1.5E-14
F8*	1.6E-14	9.4E-15	-	-	5.7E-16	3.0E-15	1.8E-14	1.2E-14

Source ID	Broad Flux	Broad Error	Soft Flux	Soft Error	Medium Flux	Medium Error	Hard Flux	Hard Error
F9	2.1E-14	1.0E-14	1.0E-14	9.0E-15	7.5E-15	4.7E-15	3.1E-15	5.4E-15
F10*	2.2E-14	1.0E-14	-	-	6.1E-15	4.3E-15	1.7E-14	1.1E-14
F11	1.1E-13	4.3E-14	7.7E-14	8.1E-14	7.7E-15	4.9E-15	2.1E-14	1.4E-14
G1	2.4E-14	1.2E-14	1.8E-15	4.0E-15	4.5E-15	4.8E-15	1.8E-14	1.2E-14
G2	1.9E-14	1.0E-14	0.0E+00	-	2.7E-15	2.9E-15	1.7E-14	1.1E-14
G3	3.5E-14	1.7E-14	0.0E+00	-	1.8E-15	2.6E-15	3.4E-14	1.8E-14
G4	1.8E-14	9.3E-15	1.1E-15	2.4E-15	1.8E-15	2.5E-15	1.6E-14	9.3E-15
G5	2.4E-14	1.1E-14	0.0E+00	-	7.3E-15	4.7E-15	1.8E-14	1.1E-14
G6*	1.6E-14	8.4E-15	-	-	1.4E-15	2.1E-15	1.5E-14	9.3E-15
G7	2.1E-13	8.9E-14	1.8E-13	2.7E-13	9.6E-15	6.2E-15	2.3E-14	1.4E-14
H1	7.6E-14	2.1E-14	4.7E-15	6.7E-15	7.6E-15	4.4E-15	6.5E-14	2.2E-14
H2*	4.5E-11	3.2E-11	4.4E-11	-	-	-	5.2E-14	3.2E-14
H3	1.4E-14	7.4E-15	0.0E+00	-	4.2E-15	3.3E-15	9.9E-15	7.5E-15
H4*	-	-	-	-	6.8E-15	5.5E-15	4.6E-14	2.8E-14
I1*	-	-	-	-	5.0E-15	4.6E-15	1.5E-13	3.5E-14
I2*	-	-	-	-	3.7E-15	4.4E-15	2.1E-14	1.5E-14
I3*	-	-	-	-	5.8E-15	4.1E-15	1.0E-14	8.0E-15
I4	7.8E-14	2.1E-14	0.0E+00	-	6.7E-15	4.8E-15	7.5E-14	2.2E-14
I5	8.8E-14	2.4E-14	1.8E-15	3.9E-15	6.0E-15	4.0E-15	8.2E-14	2.5E-14
J1*	1.1E-14	3.2E-15	-	-	1.7E-14	7.3E-15	5.4E-14	2.4E-14
K1*	-	-	-	-	7.9E-16	2.0E-15	4.2E-14	1.9E-14
K2*	-	-	-	-	9.4E-15	7.4E-15	4.9E-14	2.2E-14
K3	2.5E-14	1.2E-14	6.2E-15	8.5E-15	3.5E-15	3.9E-15	1.6E-14	9.6E-15
K4	3.0E-14	1.2E-14	6.3E-15	6.7E-15	8.0E-15	4.8E-15	1.5E-14	9.3E-15
K5	2.6E-14	1.3E-14	0.0E+00	-	8.3E-16	1.8E-15	2.6E-14	1.4E-14

Source ID	Broad Flux	Broad Error	Soft Flux	Soft Error	Medium Flux	Medium Error	Hard Flux	Hard Error
K6*	-	-	-	-	3.0E-15	3.0E-15	1.2E-14	8.3E-15
K7	3.7E-14	1.5E-14	1.6E-15	3.2E-15	3.4E-15	2.9E-15	3.3E-14	1.6E-14
K8*	7.7E-13	2.7E-13	7.4E-13	2.9E-13	4.4E-15	3.4E-15	-	-
K9	3.3E-14	1.3E-14	3.4E-15	6.9E-15	6.6E-15	4.2E-15	2.4E-14	1.2E-14
K10*	4.7E-13	5.6E-14	-	-	5.3E-14	1.3E-14	4.4E-13	5.9E-14
K11	1.5E-14	7.6E-15	5.4E-15	5.5E-15	5.9E-15	4.0E-15	3.8E-15	4.9E-15
K12*	-	-	-	-	1.5E-14	7.2E-15	2.8E-14	1.7E-14
K13	3.6E-14	1.3E-14	1.6E-14	1.1E-14	1.2E-14	5.8E-15	7.9E-15	6.8E-15
K14	5.0E-14	1.6E-14	0.0E+00	-	5.2E-15	3.9E-15	4.6E-14	1.7E-14
K15	2.4E-14	1.2E-14	1.6E-14	1.4E-14	5.4E-15	3.7E-15	2.0E-15	4.5E-15
K16	1.7E-13	3.2E-14	2.5E-14	2.3E-14	2.7E-14	8.5E-15	1.2E-13	3.0E-14
L1*	-	-	-	-	1.2E-14	8.0E-15	9.5E-15	9.8E-15
L2	4.3E-12	2.1E-12	4.2E-12	5.5E-12	5.7E-15	5.0E-15	3.4E-14	2.4E-14
L3	3.1E-14	1.4E-14	0.0E+00	-	5.0E-15	4.4E-15	2.7E-14	1.5E-14
L4	3.9E-14	1.4E-14	1.3E-14	1.2E-14	1.1E-14	5.4E-15	1.6E-14	1.0E-14
L5	5.5E-14	2.8E-14	3.7E-14	5.1E-14	2.7E-15	2.8E-15	1.4E-14	9.7E-15
L6*	5.2E-15	2.2E-15	-	-	2.3E-15	2.9E-15	2.2E-14	1.2E-14
M1	5.1E-14	2.0E-14	3.8E-14	2.6E-14	1.1E-14	5.2E-15	1.3E-15	2.2E-15
M2	3.0E-14	1.5E-14	0.0E+00	-	2.7E-15	2.8E-15	2.8E-14	1.7E-14
M3	2.0E-14	1.1E-14	0.0E+00	-	2.0E-15	2.4E-15	1.9E-14	1.2E-14
M4	5.5E-14	3.2E-14	8.2E-15	2.5E-14	1.4E-15	2.6E-15	4.6E-14	2.9E-14
M5	3.4E-14	1.2E-14	0.0E+00	-	2.3E-15	2.4E-15	3.3E-14	1.3E-14
M6	2.6E-14	1.3E-14	0.0E+00	-	1.0E-15	2.2E-15	2.6E-14	1.4E-14
M7*	1.9E-14	1.2E-14	-	-	-	-	3.2E-14	1.7E-14
M8	6.6E-14	2.0E-14	0.0E+00	-	5.5E-15	3.6E-15	6.2E-14	2.1E-14

Source ID	Broad Flux	Broad Error	Soft Flux	Soft Error	Medium Flux	Medium Error	Hard Flux	Hard Error
M9	2.3E-13	3.7E-14	3.8E-14	3.6E-14	1.0E-14	4.9E-15	1.9E-13	3.2E-14
M10*	-	-	-	-	2.8E-15	3.5E-15	4.3E-14	2.7E-14

Table 10: List of all 100 sources, which observatory they have multi-wavelength data from (2=2MASS, G-GAIA, W=WISE, P=PanSTARRS, and S=SDSS), observation exposure time, soft and hard color (hardness ratios) with their color errors.

Source ID	Fermi	MW Data	Exposure Time (s)	Soft Color	Soft Color Error	Hard Color	Hard Color Error
A1	0	G	9920	0.77	0.60	0.56	0.25
A2	0		9920	1.00	0.36	0.87	0.12
A3	0		9920	0.76	0.18	-0.56	0.21
A4	34	2,G,W	9920	0.71	0.26	-0.33	0.31
A5	0		9920	1.00	0.00	0.69	0.18
A6	0		9920	1.00	0.00	0.22	0.17
A7	0	2,G,W	9920	0.09	0.30	-0.53	0.31
A8	0	W	9920	1.00	0.03	0.42	0.16
A9	0		9920	0.42	0.46	0.31	0.32
B1	0	2	9765	-0.26	0.65	0.56	0.47
B2	0	2,G,W.P	9765	0.53	0.21	-0.40	0.22
B3	0		9765	1.00	0.21	0.80	0.14
B4	0		9765	0.76	0.30	0.11	0.31
B5	0		9765	0.93	0.15	0.38	0.15
B6	0	2,G,W.P	9765	0.36	0.48	0.30	0.34
C1	0		9926	0.85	0.30	0.55	0.18
C2	0		9926	0.48	0.49	0.50	0.25
C3	0	G	9926	0.60	0.29	-0.13	0.31
C4	0		9926	0.26	2.21	0.96	0.08
D1	0		9929	0.58	1.06	0.78	0.23
D2	0	G	9929	-0.04	0.76	0.61	0.44
D3	0		9929	-0.16	0.63	0.89	0.11
D4	0	2,G	9929	0.70	0.22	0.42	0.15

Source ID	Fermi	MW Data	Exposure Time (s)	Soft Color	Soft Color Error	Hard Color	Hard Color Error
D5	0		9929	0.20	0.51	0.51	0.28
D6	0		9929	1.00	0.00	0.79	0.12
D7	0		9929	0.72	0.27	0.68	0.11
D8	0		9929	1.00	0.07	0.51	0.23
D9	0		9929	0.64	0.34	0.51	0.18
D10	4	G,P	9929	0.56	0.45	0.60	0.21
D11	0		9929	1.00	0.00	0.73	0.18
D12	0		9929	-0.02	0.32	-0.44	0.48
E1	0	W	9926	-1.00	1.24	1.00	0.03
E2	0		9926	1.16	0.22	0.68	0.24
E3	0	2,G,W	9926	0.00	0.33	-0.74	0.33
E4	0	G	9926	1.00	0.12	0.50	0.24
E5	0		9926	1.00	0.00	0.04	0.20
E6	0		9926	0.60	0.26	-0.32	0.34
E7	0	G	9926	1.00	0.00	0.57	0.22
E8	0	2,G,W	9926	0.88	0.12	0.60	0.09
E9	0	2,G,W	9926	1.14	0.10	-0.07	0.31
F1	0		9926	1.00	1.82	0.96	0.12
F2	0	2,G	9926	0.41	0.30	0.24	0.24
F3	0	2,G	9926	0.25	0.22	0.19	0.18
F4	0	G	9926	-1.00	0.36	1.00	0.04
F5	0	2,G	9926	0.75	0.24	-0.55	0.28
F6	0		9926	1.64	0.65	0.45	0.31
F7	34	G	9926	0.45	0.27	0.35	0.19
F8	0		9926	-0.67	0.80	0.92	0.22

Source ID	Fermi	MW Data	Exposure Time (s)	Soft Color	Soft Color Error	Hard Color	Hard Color Error
F9	0	2,G,W	9926	0.32	0.28	-0.68	0.28
F10	0	2,G,W	9926	1.00	0.05	0.08	0.28
F11	0		9926	0.44	0.28	0.07	0.26
G1	0		9929	0.50	0.43	0.31	0.32
G2	34		9929	1.00	0.00	0.40	0.29
G3	0		9929	1.00	0.00	0.68	0.22
G4	3		9929	0.30	0.57	0.64	0.25
G5	3		9929	1.00	0.00	0.07	0.26
G6	0	W	9929	0.33	0.63	0.65	0.26
G7	0		9929	0.62	0.28	0.08	0.26
H1	0	P,S	9948	0.65	0.24	0.47	0.15
H2	0	P	9948	0.00	0.00	1.00	0.27
H3	0	2,G,W,P,S	9948	1.00	0.00	0.06	0.31
H4	0		9948	0.52	0.39	0.41	0.25
I1	0		9907	1.00	0.47	0.84	0.08
I2	0		9907	1.00	0.67	0.50	0.31
I3	0		9907	0.75	0.27	-0.04	0.30
I4	34		9907	1.00	0.00	0.67	0.12
I5	0		9907	0.75	0.24	0.62	0.13
J1	0	2,G	9920	0.61	0.19	0.00	0.19
K1	0		9923	1.00	0.31	0.90	0.13
K2	0		9923	0.90	0.35	0.49	0.20
K3	0	G	9923	0.19	0.47	0.50	0.28
K4	0	2,G,W	9923	0.47	0.27	-0.01	0.25
K5	3	G	9923	1.00	0.00	0.83	0.18

Source ID	Fermi	MW Data	Exposure Time (s)	Soft Color	Soft Color Error	Hard Color	Hard Color Error
K6	3		9923	0.55	0.45	0.33	0.32
K7	3		9923	0.60	0.36	0.50	0.22
K8	3	2,G,W	9923	-0.54	0.18	-1.00	0.03
K9	3		9923	0.75	0.23	0.17	0.24
K10	0		9923	1.00	0.01	0.55	0.06
K11	3	2,G	9923	0.33	0.32	-0.51	0.31
K12	0	2,G,W	9923	0.62	0.21	-0.13	0.23
K13	0	2,G,W	9923	0.29	0.23	-0.47	0.23
K14	0		9923	1.00	0.00	0.60	0.16
K15	0	2,G,W	9923	0.20	0.31	-0.75	0.27
K16	0	G	9923	0.75	0.12	0.27	0.11
L1	0	2,G,W.P	9926	0.86	0.27	-0.33	0.32
L2	0		9926	0.34	0.40	0.34	0.29
L3	0	G,P	9926	1.00	0.00	0.43	0.24
L4	0	2,G,W.P	9926	0.47	0.23	-0.22	0.23
L5	3		9926	0.20	0.44	0.33	0.31
L6	0		9926	-0.18	0.43	0.65	0.22
M1	0	2,G,W	10617	0.27	0.23	-0.78	0.20
M2	3		10617	1.00	0.00	0.45	0.27
M3	34	G	10617	1.00	0.00	0.51	0.28
M4	0		10617	0.34	1.03	0.77	0.26
M5	3		10617	1.00	0.00	0.71	0.15
M6	3		10617	1.00	0.00	0.82	0.17
M7	0		10617	0.00	0.00	1.00	0.05
M8	0		10617	1.00	0.00	0.55	0.15

Source ID	Fermi	MW Data	Exposure Time (s)	Soft Color	Soft Color Error	Hard Color	Hard Color Error
M9	0	2,G	10617	0.54	0.21	0.76	0.06
M10	0		10617	1.00	0.78	0.60	0.27

WORKS CITED

(HEASARC), NASA High Energy Astrophysics Science Archive Research Center. "HEAsoft: Unified Release of FTOOLS and XANADU." *Astrophysics Source Code Library.* Astrophysics Source Code Library, Aug 2014. ascl:1408.004.

Abdollahi, S., and et al. "Fermi Large Area Telescope Fourth Source Catalog." *The Astrophysical Journal Supplement Series* (American Astronomical Society) 247, no. 1 (2020): 33.

Aliu, E., et al. "Observation of Pulsed gamma-Rays Above 25 GeV from the Crab Pulsar with MAGIC." *Science* (American Association for the Advancement of Science (AAAS)) 332 (Nov 2008): 1221-1224.

Atwood, W. B., et al. "The Large Area Telescope on the Fermi Gamma-Ray Space Telescope Mission." *The Astrophysical Journal* (American Astronomical Society) 697 (May 2009): 1071-1102.

Boch, Thomas, and P. Fernique. "Aladin Lite: Embed your Sky in the Browser." Edited by N. Manset, & P. Forshay. *Astronomical Data Analysis Software and Systems XXIII.* Astronomical Society of the Pacific Conference Series, 2014. 277.

Coustal, Laurence. "What is a black hole? Searching for what can't be seen." *phys.org.* April 9, 2019. https://phys.org/news/2019-04-black-hole.html (accessed April 6, 2022).

Fruscione, Antonella, et al. "CIAO: Chandra's data analysis system." Edited by David R. Silva, & Roger E. Doxsey. *Society of Photo-Optical Instrumentation Engineers (SPIE) Conference Series.* 2006. 62701V.

Hare, Jeremy, Oleg Kargaltsev, George G. Pavlov, Blagoy Rangelov, and Igor Volkov. "Chandra Observations of the Field Containing HESS J1616-508." *The Astrophysics Journal* 841 (June 2017): 81.

Harvard-Smithsonian Center for Astrophysics. *Science Instruments.* July 02, 2019. https://chandra.harvard.edu/about/science_instruments.html (accessed April 2022).

—. "Telescope System." *Chandra X-ray Observatory.* May 13, 2012. https://chandra.harvard.edu/about/telescope_system.html (accessed April 2022).

Jin, Y. K., S. N. Zhang, and J. F. Wu. "Hardness Ratio Estimation in Low Counting X-Ray Photometry." *The Astrophysical Journal* (American Astronomical Society) 653 (Dec 2006): 1566–1570.

Joye, W. A., and E. Mandel. "New Features of SAOImage DS9." Edited by H. E. Payne, R. I. Jedrzejewski, & R. N. Hook. *Astronomical Data Analysis Software and Systems XII.* 2003. 489.

Lumen Learning. "Evolution of Massive Stars: An Explosive Finish." *Lumen.* n.d. https://courses.lumenlearning.com/astronomy/chapter/evolution-of-massive-stars-an-explosive-finish/ (accessed April 2022).

Mauch, T., et al. "SUMSS: a wide-field radio imaging survey of the southern sky - II. The source catalogue." *Monthly Notices of the Royal Astronomical Society* (Oxford University Press (OUP)) 342, no. 4 (July 2003): 1117-1130.

NASA Goddardd Space Flight Center. "Investigating Pulsar Wind Nebulae." *Fermi Gamma-ray Space Telescope.* Feb 18, 2016. https://fermi.gsfc.nasa.gov/science/eteu/pwn/ (accessed 2020).

Nasa High Energy Astrophysics Science Archive Research Center (HEASARC). "HEAsoft: Unified Release of FTOOLS and XANADU." *Astrophysics Source Code Library.* 08 2014. 1408.004.

NASA. "THE PROGENITOR OF A TYPE IA SUPERNOVA." *HubbleSite.* October 27, 2004. https://hubblesite.org/contents/media/images/2004/34/1620-Image.html?Year=2004&news=true (accessed April 2022).

Pinkau, Klaus. "History of Gamma-ray Telescopes and Astronomy." *Experimental Astronomy* 25, no. 1 (2009): 157-171.

Seward, Frederick D., and Philip A. Charles. *Ex[ploring the X-ray Universe.* 2nd. New York: Cambridge University Press, 2010.

Taylor, M. B. "TOPCAT & STIL: Starlink Table/VOTable Processing Software." Edited by P. Shopbell, M. Britton, & R. Ebert. *Astronomical Data Analysis Software and Systems XIV.* Pasadena, California, USA, 2005. 29.

The Imagine Team at NASA Goddard Space Flight Center. *Multiwavelength Astronomy.* Sept 2013. https://imagine.gsfc.nasa.gov/science/toolbox/multiwavelength2.html (accessed 2020).

Weisskopf, M. C., B. Brinkman, C. Canizares, G. Garmire, S. Murray, and L. P. Van Speybroeck. "An Overview of the Performance and Scientific Results from the Chandra X-Ray Observatory (CXO)." *Publications of the Astronomical Society of the Pacific* 114 (January 2002): 1-24.

Wilms, J., A. Allen, and R. McCray. "On the Absorption of X-Rays in the Interstellar Medium." *The Astrophysical Journal* 542 (Oct 2000): 914-924.